



**Politecnico  
di Torino**

**Politecnico di Torino**

Master's Degree in Energy and Nuclear Engineering

Master's Thesis Degree

**Application of Fiber Bragg Grating  
Sensors in Quench Detection for HTS  
BRAST-based Cables in Fusion Magnets**

Supervisor: Prof. Laura Savoldi

Supervisor: Dr. Andrea Masi

Co-supervisor: Dr. Sofia Viarengo

Candidate: Mattia De Stasio

Academic Year 2023/2024

# Abstract

*This thesis explores the integration of Fiber Bragg Grating (FBG) optical fibers as an innovative solution for quench detection in high-temperature superconducting (HTS) cables, specifically within a 6-slot aluminum core design for fusion applications developed at ENEA. HTS materials, such as REBCO, are known for their high critical parameters but present challenges in quench detection due to their low normal zone propagation velocity (NZPV). Traditional voltage-based quench detection methods are less effective under these conditions, necessitating alternative solutions.*

*In this study, an HTS cable was designed and fabricated utilizing a BRAided STACK (BRAST) of REBCO tapes, incorporating FBG sensors within steel capillaries placed directly onto the stack. Experiments were conducted in both liquid nitrogen bath and flow at 77 K to promote quench events and assess the performance of FBG-based detection methods in comparison to conventional voltage taps and thermocouples. Results demonstrate that the FBG sensors provide rapid and accurate thermal response detection, allowing real-time monitoring of temperature variations within the stack. Furthermore, the study underscores the practical benefits and challenges of optical fiber integration, which is critical for durability in high-current HTS applications.*

*The findings support the viability of FBG-based quench detection in HTS cables for fusion applications, offering enhanced detection sensitivity, reduced electromagnetic interference, and valuable insights into future development of robust, high-performance superconducting magnet systems.*

# Preface

The work described in this thesis is the result of a collaboration between ENEA, Politecnico di Torino, Alma Mater Studiorum - Università di Bologna, and ENI S.p.A, to whom I extend my sincere thanks for giving me this opportunity. It was carried out in ENEA (Agenzia Nazionale per le Nuove Tecnologie, l'Energie e lo Sviluppo Economico Sostenibile) at the Frascati Research Center under the supervision of Dr. Andrea Masi and Prof. Laura Savoldi. This thesis is the results of my own work, and to the best of my knowledge does not contain material previously published or written by the other authors, except where due reference is indicated in the text.

This work is conducted in the framework of the EU-DEMO EUROfusion program [1]: in particular, it investigates the application of the FBGs optical fiber as instrumentation for quench detection in the superconducting cable for the central solenoid.

This thesis does not contain any material which has been previously submitted for the award of degree or other qualification to any university or institution. Parts of this work presented in this thesis has been submitted for publication in "Masi, A., Colombo, G., De Stasio, M., Breschi, M., Caponero, M. A., Celentano, G., Marchetti, M., Muzzi, L., Polimadei, A., Savoldi, L., Trotta, A., Zanon, F., & De Marzi, G. (submitted). *Integration of Optical Sensors for Quench Detection in HTS Stacks and Cables for Fusion Applications*. <http://ieeexplore.ieee.org>".

# Table of Contents

1. Introduction .....	6
1.1 Superconducting Cables .....	9
1.2 Quench Phenomenon .....	11
1.3 FBGs Optical Fiber for the Quench Detection .....	15
1.4 Aim of the Work.....	23
2. Sample Preparation and Experimental Setup .....	24
2.1 Sample Cable Preparation.....	25
2.1.1 Core Preparation .....	25
2.1.2 Jacketing Process .....	30
2.1.3 Optical Fiber Installation .....	31
2.2 Setup of the Experiments .....	32
3. Results and Discussion .....	36
3.1 Test in Liquid Nitrogen Bath at 77 K.....	36
3.2 Test in Liquid Nitrogen Flow at 77 K.....	40
4. Conclusion and Perspectives.....	50
Appendix A – Drawings of the Cable Design .....	51
References.....	57

# Table of Figures

<i>Figure 1.1.1: Different types of superconducting materials in their commercial forms [16]</i> .....	10
<i>Figure 1.1.2: Sketch of a REBCO tape structure [17]</i> .....	11
<i>Figure 1.2.1: Current rerouting in the stabilizer due to local loss of superconductivity</i> .....	11
<i>Figure 1.2.2: Sketch of the quench phenomenon activation and the definition of the MZP [3]</i> .....	12
<i>Figure 1.2.3: Different NZPV in LTS and HTS [19]</i> .....	13
<i>Figure 1.2.4: Power Law of NZPV in HTS [21]</i> .....	14
<i>Figure 1.2.5: Different non-voltage quench detection techniques [19]</i> .....	15
<i>Figure 1.3.1: Operation of an FBG sensor in optical fiber [22]</i> .....	16
<i>Figure 1.3.2: Variation of the Bragg wavelength with temperature change [22]</i> .....	16
<i>Figure 1.3.3: Sketch of an optical fiber coated with protective material [24]</i> .....	17
<i>Figure 1.3.4: Result data from the last heat pulse at 10 K [22]</i> .....	19
<i>Figure 1.3.5: Result data from the last heat pulse at 20 K [22]</i> .....	19
<i>Figure 1.3.6: Results data of the quench event using optical fibers at different positions and voltage taps [25]</i> .....	20
<i>Figure 1.3.7: Difference in time response of the quench detection between optical fiber and voltage taps [25]</i> .....	21
<i>Figure 1.3.8: Setup of the experiment [26]</i> .....	21
<i>Figure 1.3.9: Section of the cable with the instrumentation installed [26]</i> .....	22
<i>Figure 1.3.10: Results of the quench induced experiment [26]</i> .....	22
<i>Figure 2.1.1: Sketch of the aluminum 5-slot core section. The measures are reported in millimeters.</i> ..	25
<i>Figure 2.1.2: Sketch of the structure section of the BRAST: the (1) stack is positioned within the (2) braid tin structure and at the bottom of the (3) two steel capillaries</i> .....	26
<i>Figure 2.1.3: Sketch of the voltage tap placement on the cable: the high-field zone includes the voltage taps A1-A6, along with the symmetrical B1</i> .....	27
<i>Figure 2.1.4: Picture of the soldering process for the voltage taps in the high-field region on the BRAST</i> .....	27
<i>Figure 2.1.5: BRAST integrated into the aluminum core with the voltage taps in the high-field zone</i> ..	27
<i>Figure 2.1.6: Staggered 15 mm notches on the tapes for pre-soldering</i> .....	28
<i>Figure 2.1.7: Rendering of the end portion of the core with its components [35]</i> .....	29
<i>Figure 2.1.8: Final result of the pre-soldering process of the tapes (on the left) and the soldering process with the copper rod (in the center and on the right)</i> .....	29
<i>Figure 2.1.9: Wrapped thin layers of stainless steel around the core before the jacketing process</i> .....	30
<i>Figure 2.1.10: Details of the wire-drawing process with one of the brass jigs used</i> .....	30
<i>Figure 2.1.11: Result of the jacketing process</i> .....	31
<i>Figure 2.1.12: Completed sample cable with the copper terminations installed</i> .....	31
<i>Figure 2.1.13: Fiber Bragg Grating optical fiber used (on the left) and a detail of the optical fiber within the stainless-steel capillary on the center). Structure to house optical fiber in the sample setup on the right)</i> .....	32
<i>Figure 2.2.1: Photo of the FATA 20kA power supply used and the instrumentation station</i> .....	33
<i>Figure 2.2.2: Details of the CERNOX thermocouples setup on the surface of the aluminum jacket</i> .....	34
<i>Figure 2.2.3: Response of the CERNOX thermocouples (a) and the FBGs array (b) during the heating transitory to evaluate the sensitivity in terms of relation between <math>\Delta\lambda - \Delta T</math></i> .....	34
<i>Figure 2.2.4: Details of the inflow setup experiment (on the left and on the center). Details of the bath experiment (on the right)</i> .....	35
<i>Figure 3.1.1: Voltage signals from the tapes in LN bath</i> .....	36
<i>Figure 3.1.2: Voltage signals from the core and terminations in LN bath</i> .....	37

<i>Figure 3.1.3: IV curve of 1B-2B with curve fit in LN bath.....</i>	<i>37</i>
<i>Figure 3.1.4: IV curve of 2A-1A with curve fit in LN bath.....</i>	<i>38</i>
<i>Figure 3.1.5: The response of voltage taps (a) and FBGs (b) in LN bath. (c) Detail of the FBGs response.....</i>	<i>39</i>
<i>Figure 3.2.1: Cooling transitory measured from the CERNOX thermocouples on the aluminum jacket surface.....</i>	<i>40</i>
<i>Figure 3.2.2: Pictures of the LN flow setup during the experiment: (a) the detail of the copper termination B, (b) the stainless steel capillary and the optical fiber and (c) upper view of the cable setup [35].....</i>	<i>41</i>
<i>Figure 3.2.3: Voltage signals from the tapes in LN flow.....</i>	<i>41</i>
<i>Figure 3.2.4: Voltage signals from the core and terminations in LN flow.....</i>	<i>42</i>
<i>Figure 3.2.5: Detail of the first quench detected, and the response of voltage tap (a) and FBGs (b) in LN flow.....</i>	<i>43</i>
<i>Figure 3.2.6: Detail of the second quench detected, and the response of voltage tap (a) and FBGs (b) in LN flow.....</i>	<i>43</i>
<i>Figure 3.2.7: Detail of the third quench detected, and the response of voltage tap (a) and FBGs (b) in LN flow.....</i>	<i>44</i>
<i>Figure 3.2.8: Temperature acquired by the CERNOX during the first (a), second (b) and third (c) quench events.....</i>	<i>45</i>
<i>Figure 3.2.9: New configuration for the FBGs array position.....</i>	<i>45</i>
<i>Figure 3.2.10: Different FBGs position for the evaluation of defect location: (a) FBGs array towards +0.5 cm to Termination A, (b) towards +1.0 cm, (c) towards +2.0 cm and (d) towards +2.5 cm.....</i>	<i>46</i>
<i>Figure 3.2.11: Response of the FBGs during one of the main quenches: (a) the results of different coating cross-section on sensitivity (the single FBG went off-scale), (b) the detail of the FBG array response during the quench event.....</i>	<i>47</i>
<i>Figure 3.2.12: Current rump of the two experiments run for the NZPV computation.....</i>	<i>48</i>
<i>Figure 3.2.13: Time derivative of the FBGs signals: the points highlighted represent the time in which the signal slope increases and starts the thermal runaway.....</i>	<i>48</i>

# 1. Introduction

Superconductivity is the physical phenomenon by which a conductor can carry an electric current without any resistance, below a temperature known as the critical temperature or transition temperature. The discovery of superconductivity credits to Heike Kamerlingh Onnes in 1911, during his experimental campaign to measure the resistivity of certain metals. In the process of obtaining a pure form of mercury through repeated distillations, he found that at a temperature of 4.2 K, the electrical resistance of mercury dramatically dropped to zero. Onnes thus introduced a new state of matter, which he named 'superconductivity,' earning him the Nobel Prize in Physics in 1913. From that point on, the scientific community began a long series of experiments to determine the temperature at which this phenomenon occurred in other chemical elements [3].

Onnes realized the importance of superconducting materials for constructing high-field magnets without the large dissipation caused by current transport. However, he soon discovered that applying even an extremely low magnetic field to materials in a superconducting state caused them to revert to their normal state. It is therefore clear that, in addition to temperature, superconductivity also depends on the external magnetic field applied to the material [3].

Today, it is well-known that for a superconducting material to remain in that state, it must not exceed three important critical parameters, all of which are interdependent: the critical temperature ( $T_c$ ), the critical magnetic field ( $B_c$ ) and the critical current density ( $J_c$ ).

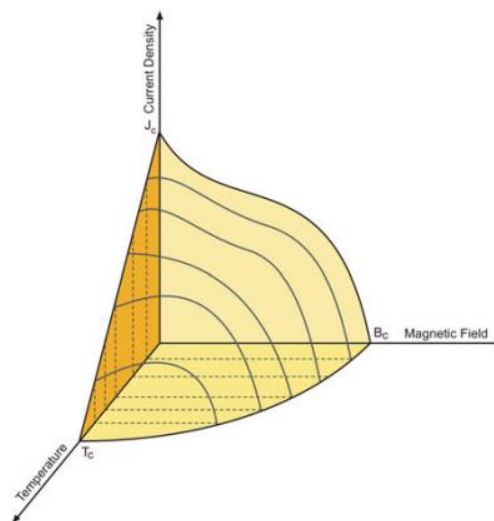


Figure 1.1: Superconductor's critical parameters define the superconductor state [3]

Critical temperatures  $T_c$  are known to range from a fraction of 1 K to slightly above 100 K. Superconductors with critical temperatures near this upper limit are commonly

referred to as high-temperature superconductors (HTS) while superconductors with critical temperatures near to the upper limit of 30 K are called low-temperature superconductors (LTS). From a practical perspective, superconductors with high  $T_c$  values hold significant importance. Presently, applications involving superconductors often necessitate immersing superconducting materials in liquid helium (at 4.2 K) to maintain them below their critical temperature. However, liquid nitrogen maintains a temperature of 77 K, making it more abundant and cost-effective compared to liquid helium. It would significantly enhance cost-effectiveness if high-temperature superconductor components could be readily fabricated and utilized, requiring only immersion in liquid nitrogen to maintain their superconducting properties.

Another important characteristic of a superconducting material is its critical magnetic field, denoted as  $B_c(T)$  which represents the maximum applied magnetic field at temperature  $T$  that permits the material to maintain superconductivity. The critical magnetic field can be approximated as:

$$B_c(T) = B_c(0 \text{ K}) \cdot \left[ 1 - \left( \frac{T}{T_c} \right)^2 \right]$$

If the applied magnetic field exceeds the critical field, it will disrupt the superconducting state. An important property that superconductors exhibit is the so-called 'Meissner effect': below its critical temperature and its critical magnetic field, the superconductor behaves like a perfect diamagnet, completely expelling the magnetic field.

There is a class distinction among superconductors based on the different values at which the expulsion of the magnetic field is observed: Type I superconductors and Type II superconductors.

Type I superconductors do not allow magnetic flux penetration for a certain value of  $B < B_c(T)$ , meaning that in the  $B - T$  phase diagram, there is a clear distinction between the region where the Meissner effect occurs and the region beyond the curve that defines the values of  $B_c(T)$ , where no magnetic field penetration occurs. Type II superconductors, on the other hand, show a substantial difference: in the phase diagram, there are two distinct curves that define the values of the lower critical field ( $B_{c1}$ ) and upper critical field ( $B_{c2}$ ), identifying three different regions. In the region below the curve where  $B < B_{c1}(T)$ , the superconductors exhibit the Meissner effect; in the region where  $B > B_{c2}$ , the Meissner effect is absent, while for the values  $B_{c2}(T) > B > B_{c1}(T)$ , there is the mixed state region, an area where partial magnetic field penetration occurs, allowing flux pinning. In general,  $B_{c2}(T)$  is large compared with the critical fields of type I superconductors, so wire made of type II superconducting material is suitable for the windings of high-field magnets.

Lastly, the critical current density  $J_c(T)$ . As mentioned before, electrical resistivity tends to be zero in the superconductive state and, as consequence, the electric field is null.

When the superconductor enters the transition region, the electric field tends to reappear according to the power law:

$$E = E_0 \cdot \left(\frac{J}{J_c}\right)^n$$

with the Criterion parameter  $E_0$  and  $n$  the n-value [4]. These two parameters are crucial for describing the superconducting behavior of materials. The  $E_0$  is linked to the transition point between the resistive and superconducting states, conventionally recognized as  $1 \mu V/cm$ , while n-value defines the nature of this transition. A high n-value corresponds to a sharp and rapid transition, which implies a more stable material that can better withstand disturbances, such as fluctuations in temperature or current. On the other hand, a lower n-value leads to a more gradual transition, indicating a material that is less stable and more sensitive to changes in operating conditions like temperature or current. [5] [6].

When one of the three parameters, current density, temperature and magnetic field, surpasses the critical threshold, a phenomenon known as current sharing occurs. In current sharing, the superconductor material accepts the critical current density, while the excess current cannot be sustained. Consequently, other non-superconductive materials must bear the excess current, leading to joule heating.

Bad cooling may result in the heating of materials, including the superconductor itself, thereby restricting its superconducting capabilities. In fact, cryogenic liquids, such as liquid helium (LHe) and liquid nitrogen (LN), play a crucial role in maintaining the superconducting state of materials [7]. For low-temperature superconductors, this temperature is often extremely low, requiring liquid helium at 4.2 K to maintain the superconducting phase. In the case of high-temperature superconductors, liquid nitrogen, which cools to 77 K, can often be used, though lower temperatures are sometimes needed for optimal performance.

Efficient cryogenic cooling is essential because it not only ensures that the material stays below its critical temperature and has a sufficient thermal margin but also helps manage the heat generated during operation. It is necessary also to consider that the use of cryogenic liquids significantly contributes to the operational costs and energy consumption in superconducting systems: cooling to cryogenic temperatures requires substantial energy, especially for low temperature superconductors. Maintaining these temperatures involves continuous replenishment of cryogens, along with the energy-intensive cooling infrastructure required to prevent losses. The high temperature superconductors offer a more cost-effective alternative due to lower cooling requirements [7].

# 1.1 Superconducting Cables

Superconducting materials are used in several sectors [8] [9] [10] [11] [12] [13] [14]. They are especially prominent in scientific research, where they are employed in particle accelerators and fusion reactors as high-field magnets. Additionally, there is a growing trend in the energy transmission market, in magnetic levitation transport (Maglev), in the electric motors and generators sector, and in the medical field with MRI machines. [2].

Over the years, increasingly advanced techniques have been developed to produce superconducting cables, utilizing several types of LTS and HTS. The table below summarizes the main superconducting materials used in industry.

Table 1.1.1: Main superconductor materials used in the application sectors [2]

Material	$T_c$ (K)	$H_{c2@4.2K}$ (T)	$J_{c@4.2K,0T}$ ( $\frac{A}{m^2}$ )	Wire technology	Typical wire form
Nb-Ti (LTS)	9.5	11.5	4E5	-	Round wire
Nb <sub>3</sub> Sn (LTS)	18	25	1E6	Bronze process, internal Sn process, powder-in-tube	Round wire
MgB <sub>2</sub> (HTS)	39	18	1E6	Powder-in-tube, internal Mg diffusion	Wire or tape
REBCO (HTS)	92	>100	1E7	Coated conductor	Flat tape
Bi-2223 (HTS)	108	>100	1E6	Powder-in-tube	Flat tape
Bi-2212 (HTS)	90	>100	1E6	Powder-in-tube	Wire or tape

In sectors where there is a need to reduce operative costs and make applications economically scalable, HTS are predominantly studied for perspective use due to their much higher critical parameters and higher performance compared to LTS [15]. Particularly promising are Rare-Earth-Barium-Copper-Oxygen (REBCO) tapes, especially the YBCO type, which contains Yttrium.

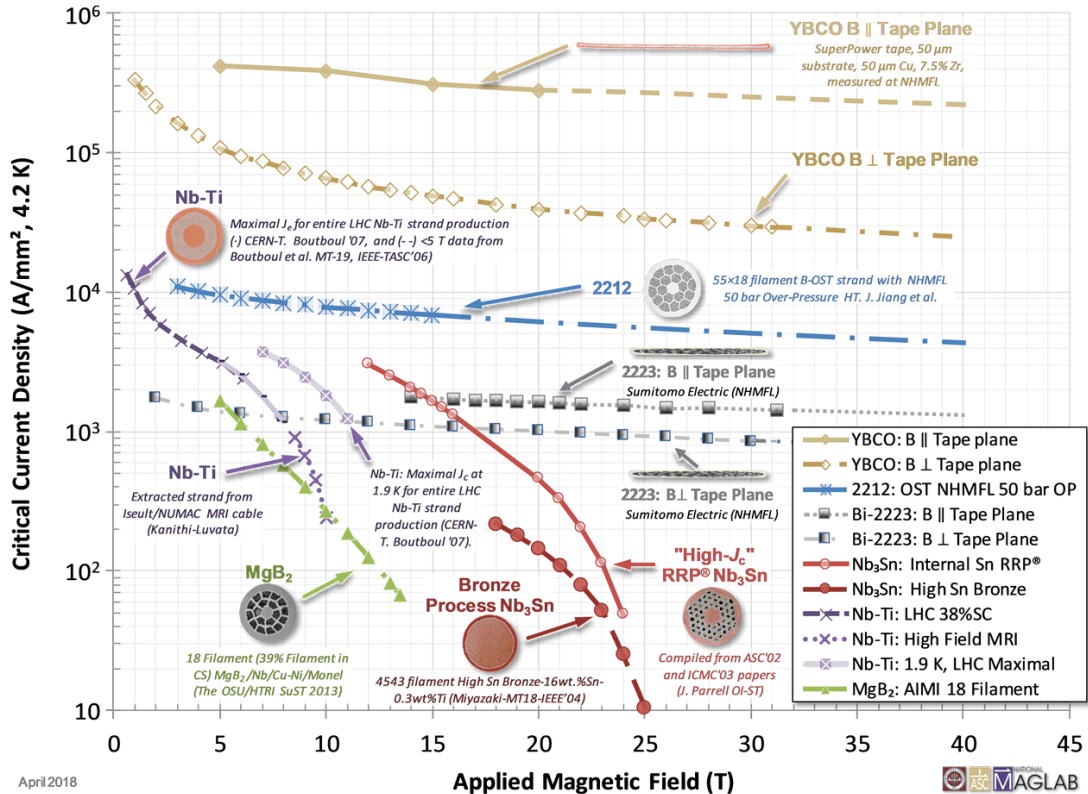


Figure 1.1.1: Different types of superconducting materials in their commercial forms [16]

By [17] can be noticed that in recent times, advancements in the research of second-generation (2G) YBCO coated conductor (CC) tapes have been noteworthy. These tapes exhibit the capability to carry high current densities either at temperatures of up to 77 K under self-field conditions or at low temperatures in high magnetic fields exceeding 20 T. To achieve high critical current densities, it is imperative to establish a robust biaxial texture within the superconductor. To this end, various layers, known as buffer layers, are applied onto a biaxially textured metallic substrate. These buffer layers serve the dual purpose of enhancing texture and grain orientation while also inhibiting diffusion from the metal substrate into the superconducting YBCO layer. Given that numerous applications necessitate robust mechanical support, it is imperative that the substrate exhibits a high responsiveness to both axial and bending stresses. To meet stability standards, it is necessary to incorporate metallic stabilizer layers (Silver or Copper) on each side of the tape. This enhances the tape's capacity to carry both current and heat should it transition to a normal state.

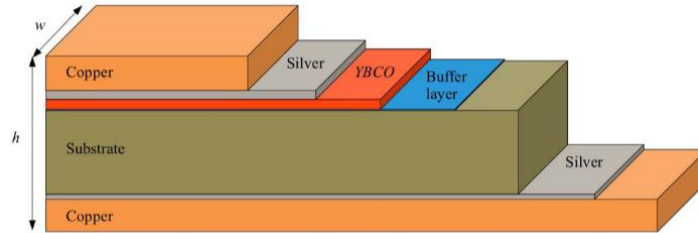


Figure 1.1.2: Sketch of a REBCO tape structure [17]

When this occurs, heat generation occurs due to the Joule heating and a local hot spot may form, which could lead to the degradation of the superconducting state into the normal state. This phenomenon is called quench.

## 1.2 Quench Phenomenon

Quench is the phenomenon when, suddenly, a portion of the superconductor turns resistive during the operation. The Joule heating generated locally in the initial resistive area can propagate along the entire cable, causing overheating and leading to a further rise in temperature, exacerbating the event. The entity of the quench phenomenon can be minimized by stabilizing the cable through the appropriate core stabilizer such as Aluminum or Copper and designing it to reroute the current flow in a parallel path, since in the normal state the superconductor has high electrical resistivity and low thermal conductivity. In this context, the ability of cryogenic liquids to rapidly absorb heat and dissipate it is critical for the stability and performance of superconducting systems. Maintaining proper cryogenic conditions is, therefore, vital to avoid quench events and ensure the reliable operation of superconductors, especially in demanding applications like power cables or magnets in fusion reactors.

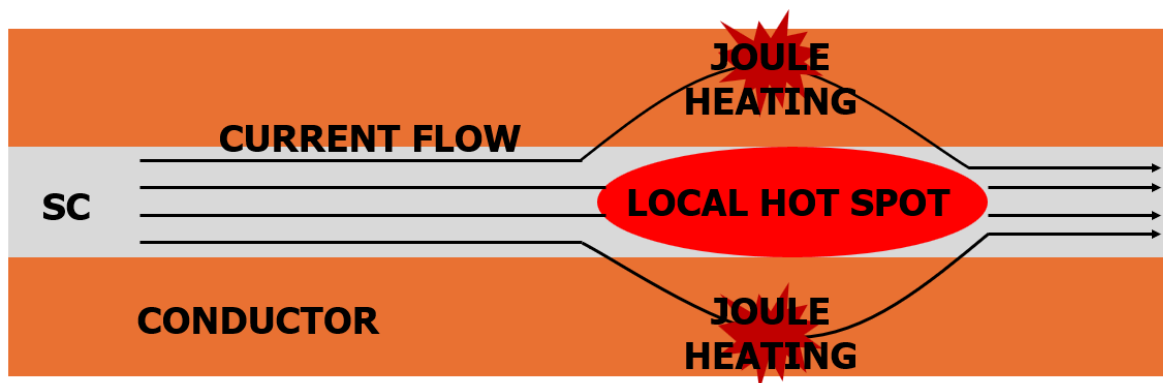


Figure 1.2.1: Current rerouting in the stabilizer due to local loss of superconductivity

Considering a sudden local heat pulse, the heat will travel through a conductor longitudinally in both directions at a rate depending on the materials thermal conductivity. If the heat generated at the 'hot spot' is dissipated more quickly than it is

produced, the normal zone will shrink, stabilizing the cable. However, if heat dissipation is slower, the normal zone will expand and spread throughout the adjacent zones, leading to the quenching of the cable.

There is a portion of the normal zone, called minimum propagation zone (MPZ) in which the quench phenomenon initiates.

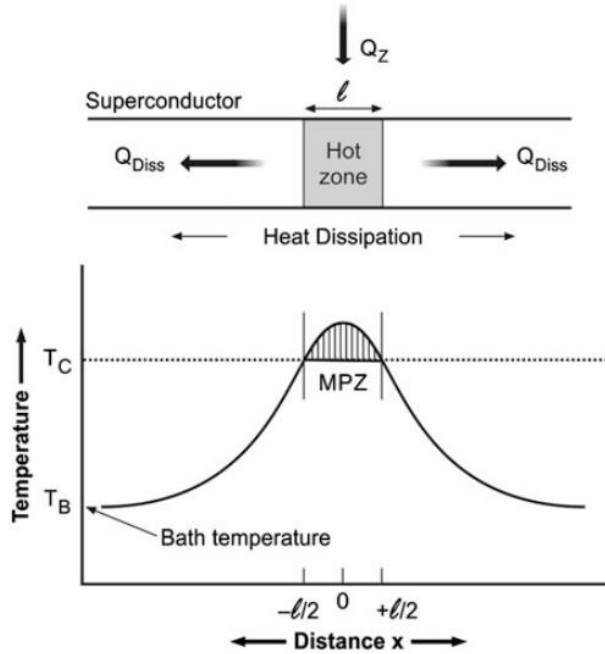


Figure 1.2.2: Sketch of the quench phenomenon activation and the definition of the MZP [3]

Considering a generic section  $A$  of the conductor containing superconductor material, the generating heat due to Ohmic heating in normal zone can be defined as:

$$Q_g = \rho_{el} \cdot J^2 \cdot A \cdot l$$

with  $\rho_{el}$  the electrical resistivity of the superconductor in the normal state and  $l$  the length in which the local hot spot occurs. The heat conduction in the two directions along the cable can be defined as:

$$Q_d = 2 \cdot \frac{k \cdot A \cdot (T_c - T_{cooler})}{l}$$

with  $k$  the thermal conductivity of the conductor and  $T_{cooler}$  the temperature of the cooling liquid.

If the energy balance is performed [18], it is possible to obtain the expression for  $l$ :

$$l = \sqrt{\frac{2 \cdot k \cdot (T_c - T_{cooler})}{J^2 \cdot \rho_{el}}}$$

This parameter defines the quench propagation: when the size of the hot zone is less than  $l$ , the heat generated will dissipate away, depending on the materials' properties and the temperature of the liquid cooling, and the hot spot will disappear. By contrast, if the size exceeds  $l$ , the quench will grow and propagate. The parameter that determines the extent of quench propagation along the cable is known as the Normal Zone Propagation Velocity (NZPV). It represents the speed at which the resistive zone progresses through the superconducting cable during a quench, indicating how rapidly the region where the material loses its superconducting properties expands. It depends on heat dissipation, the efficiency of the cooling system and the thermal and electrical properties of the superconductor. There is a significant difference between LTS and HTS in terms of NZPV: typical NZPV values for LTS range from 10 to 40 m/s, whereas for HTS, they are much lower, around 2 to 40 cm/s [11] [19].

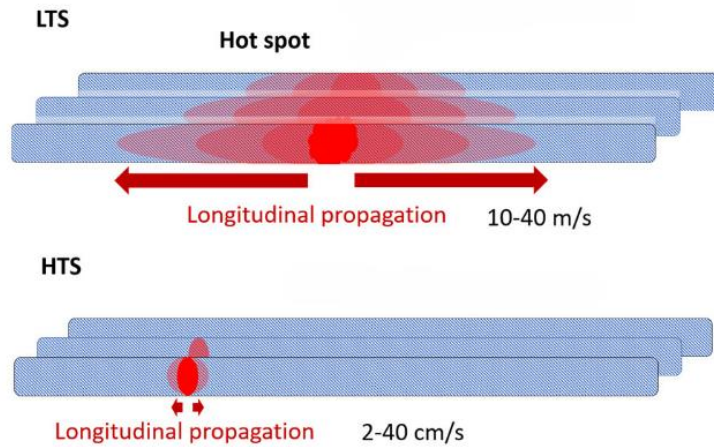


Figure 1.2.3: Different NZPV in LTS and HTS [19]

To describe qualitatively the effect of the different NZPV in HTS and LTS and why it is relevant in the quench detection, it is necessary to consider the heat balance per unit volume in adiabatic condition [20]:

$$\int_{T_{op}}^{T_{MAX}} \frac{\gamma C_p(T)}{\rho_{el}(T, B)} dT = \int_{t_1}^{t_2} J^2 dt$$

It is known that HTS has a wider temperature margin, which translates to a greater energy margin, as shown on the left side of the previous equation, that benefits the cable's operation until a quench occurs. In such a case, the hotspot temperature is significantly higher than that of the LTS, and the low NZPV, considering also that the thermophysical properties of HTS do not guarantee effective heat distribution

compared to LTS, as most HTS materials are composed of ceramics, may not be sufficient to propagate the quench throughout the superconductor, making timely detection of the issue more challenging.

An experiment campaign conducted by J. van Nugteren [21] has shown the correlation between the three parameters (temperature, magnetic field and current) and the NZPV in a REBCO coated conductor (HTS). In the figure 1.2.4, the results are presented:

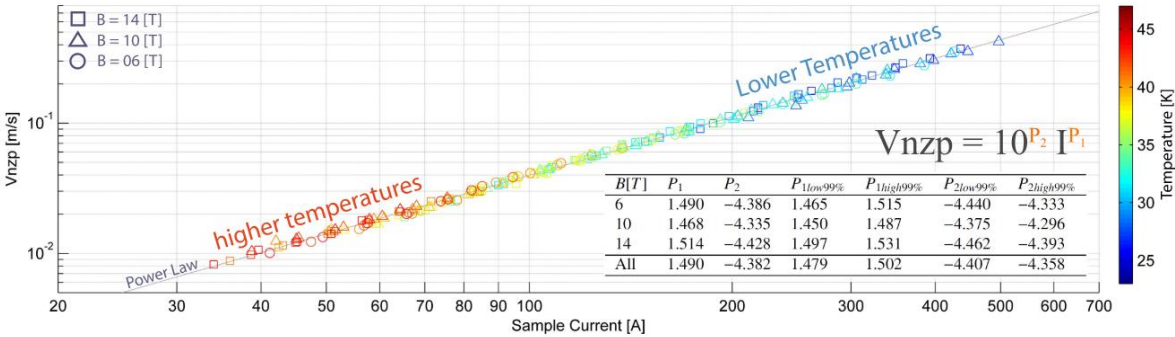


Figure 1.2.4: Power Law of NZPV in HTS [21]

The graph shows that at lower temperatures, the propagation of the normal zone is faster, while higher temperatures reduce the propagation speed. This reinforces the challenge of operating at higher temperatures to reduce operational costs, as detecting a quench becomes more difficult.

There are numerous methods for quench detection, with the most used one being the monitoring of voltage across the conductor. By installing voltage taps along the superconductor, it is possible to detect potential hotspots caused by the increased resistance during a quench. In the superconducting state, the voltage remains zero due to the absence of resistance, but when a quench occurs, the voltage rises because of the transition out of the superconducting state and the redistribution of current into the stabilizer.

While this method is simple and effective, it presents several challenges. The crucial issues are the influence of the measurement by the electromagnetic noise created the difficulty of monitoring every point along the cable, as a quench can be triggered by intrinsic defects in the material that are hard to detect. Additionally, this method cannot precisely determine the location or magnitude of the quench over time, which limits its ability to provide detailed, real-time information on the progression of the event. In addition, in the HTS, the quench propagates over a smaller region due to its NZPV, which limits the voltage rise along the conductor, making it harder for voltage taps to detect the event promptly. As a result, the quench may go unnoticed until it has spread further, delaying detection and response.

As a result, alternative or complementary detection techniques may be required to ensure more accurate and comprehensive quench detection. The most used are presented below [19]:

- **Magnetic techniques:** these are based on detecting the temporal variation of the magnetic field near a developing quench.
- **Optical techniques:** these rely on detecting changes in the optical properties of the fiber due to local thermal expansion (thus temperature detection) or thermally induced strain variation.
- **Acoustic techniques:** these utilize externally generated acoustic waves to probe changes in the cable.
- **Capacitive techniques:** This method monitors the capacitance between two structural elements of an HTS separated by an insulating layer that is partially or fully impregnated with a cryogenic liquid.
- **RF-based techniques.**

Magnetic Techniques	Quench Antennas
	Hall Sensor Arrays
Optical techniques	Fiber Bragg grating sensors
	Rayleigh scattering
	Raman scattering, Brillouin scattering and specialized fibers
Acoustic techniques	Passive (acoustic emission)
	Active (diffuse wave ultrasonics)
Capacitive techniques	Boiling of cryogenic liquids
RF-based techniques	Impedance change
	Time-frequency domain reflectometry

*Figure 1.2.5: Different non-voltage quench detection techniques [19]*

In the context of this thesis, the quench detection technique using optical fibers, with Fiber Bragg Grating sensors, will be analyzed in detail, focusing on their implementation in a potential superconducting cable design developed by ENEA for the central solenoid of the future EU DEMO fusion reactor.

## 1.3 FBGs Optical Fiber for the Quench Detection

The use of the optical fibers as an alternative approach to quench detection offers an immunity to the electromagnetic noise that affects all voltage-based methods and bases the quench detection by measuring the strain and temperature changes in optical fibers embedded within a superconducting cable.

An FBS sensor acts as a reflector: when broad-spectrum light is injected into the optical fiber containing the sensor, some of the energy is transmitted, while a portion is

reflected at a specific wavelength known as the Bragg wavelength  $\lambda_B$  which satisfies the following Bragg condition [22]:

$$\lambda_B = 2 \cdot \Lambda(T, \varepsilon) \cdot \eta_{eff}(T, \varepsilon)$$

where  $\Lambda$  (nm) is the grating period e  $\eta_{eff}$  (-) is the effective refractive index of the core. The detection of the FBS sensor is since both the grating period and the refractive index are influenced by temperature and strain, resulting in a shift of the reflected wavelength.

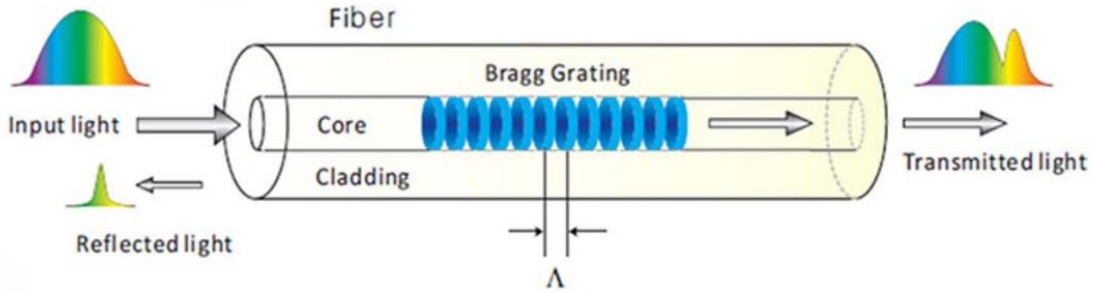


Figure 1.3.1: Operation of an FBG sensor in optical fiber [22]

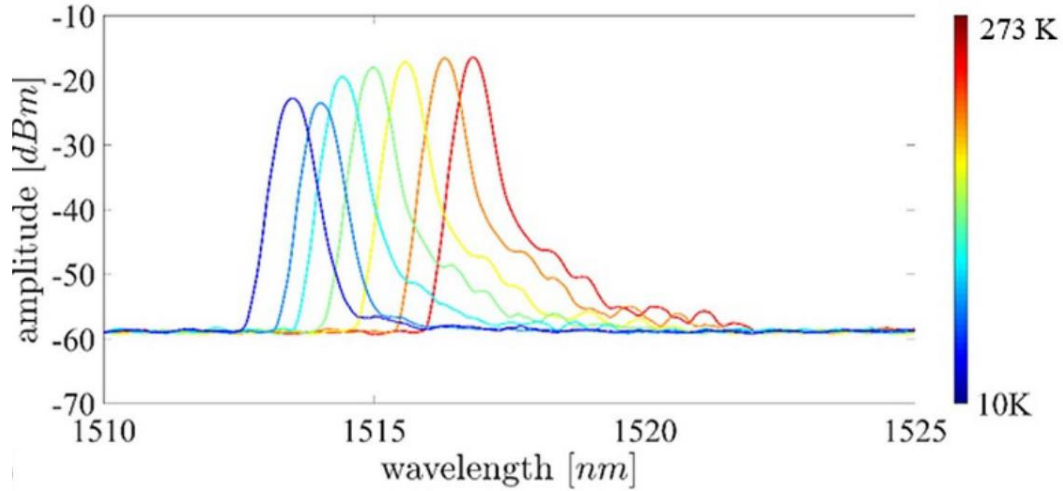


Figure 1.3.2: Variation of the Bragg wavelength with temperature change [22]

There is a proportionality between the change in temperature  $\Delta T$  and a change in length of the optical fiber  $\Delta l$  caused by external factors and the change in the Bragg wavelength defined as [23]:

$$\Delta\lambda_B = 2 \cdot \left( \eta_{eff} \frac{d\Lambda}{dT} + \Lambda \frac{d\eta_{eff}}{dT} \right) \cdot \Delta T + 2 \cdot \left( \eta_{eff} \frac{d\Lambda}{dl} + \Lambda \frac{d\eta_{eff}}{dl} \right) \cdot \Delta l$$

As the figure 1.3.2 shows, when the temperature rises the spectral peak shifts to longer wavelength due to the change of the refraction and the thermal expansion  $\alpha$  of the grating period.

Optical fibers are usually coated with a thin layer of polymeric or metallic material for protection, which plays a crucial role in their sensitivity.

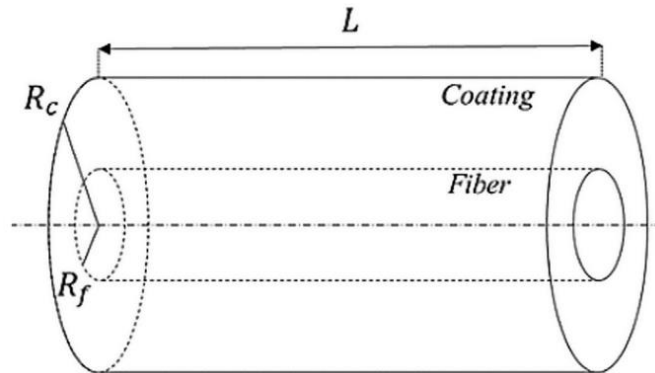


Figure 1.3.3: Sketch of an optical fiber coated with protective material [24]

Indeed, depending on the material used for the coating, the strain  $\varepsilon$ , defined as the ratio between the change in length and the initial length, will take different values due to the mechanical properties of the materials. This, in turn, differs from the strain of the optical fiber itself, which is typically made of fused silica.

The normal load to which an optical fiber is subjected is given by:

$$N_f = E_f \cdot \varepsilon_{f,mech} \cdot A_f$$

while for the coating material, it is given by:

$$N_c = E_c \cdot \varepsilon_{c,mech} \cdot A_c$$

where  $E$  is the Young modulus,  $\varepsilon_{mech}$  is the strain due solely to the mechanical stress, and  $A$  is the cross-section area related to both the fiber and the coating.

Imposing the equilibrium equation:

$$N_f + N_c = 0 \Rightarrow (E_f \cdot \varepsilon_{f,mech} \cdot A_f) + (E_c \cdot \varepsilon_{c,mech} \cdot A_c) = 0$$

The relationship between temperature variation and strain is given by:

$$\varepsilon_f = \varepsilon_{f,mech} + \alpha_f \cdot \Delta T$$

$$\varepsilon_c = \varepsilon_{c,mech} + \alpha_c \cdot \Delta T$$

By substituting the two mechanical strains into the previous two equations, and solving the general strain value:

$$\varepsilon = \left( \frac{E_f \cdot \alpha_f \cdot A_f + E_c \cdot \alpha_c \cdot A_c}{E_c \cdot A_c + E_f \cdot A_f} \right) \cdot \Delta T$$

The equation above shows that the strain depends on the material used for the coating and its dimensions [24]. An Optical Fiber Interrogation System (OFIS) will determine the values of the measured variables of temperature or strain derived from the change in wavelength. For the temperature, the signal  $S_{FBG}$  acquired by the OFIS is the following [22]:

$$S_{FBG} = \Delta\lambda_B \cdot \alpha \cdot \Delta T$$

Numerous scientific studies have explored the use of FBGs in quench detection. For instance, E. Salazar et al. [22] conducted an experiment at the SULTAN facility on the feasibility of fiber optic thermometry as quench diagnostics for VIPER [8] cables under operational conditions similar to those of a magnet. The objectives included demonstrating the capability of FBG and ULFBG (Ultra Long Fiber Bragg Grating) technologies to detect simulated quench events, as well as determining the sensitivity, response times, and operational robustness of the fibers. The research aimed to establish a foundation for a large-scale fiber optic quench detection system for HTS magnets based on VIPER cables.

Several voltage taps were installed to measure the voltage across the cable, along with CERNOX thermocouples for temperature measurement and two resistive heaters to induce localized quench events through heat pulses. The heaters were mounted directly on the copper jacket through openings in the stainless-steel jacket. The FBG and ULFBG optical fiber sensors are highly sensitive instruments. To prevent potential damage from electromagnetic forces during the experiment and material contraction during cable cooldown, the sensors were embedded in finely machined grooves within the copper jacket. The ULFBG sensors were fully embedded with epoxy resin (Stycast 2850FT), while the FBG sensors were covered partially with the same epoxy resin and with Kapton.

The graphs below show the latest heat pulse induced by the resistive heaters at 10 K, 10.9 T, with an operating-to-critical current ratio of approximately 0.9 (Figure 1.3.4), and the latest heat pulse at 20 K, 10.9 T, with an operating-to-critical current ratio close to 1.0 (Figure 1.3.5). In both cases, for both FBGs and ULFBGs, the detected signal demonstrates clear responses to the heater pulses leading up to the quench event, as well as a strong reaction to the quench itself at the end of the test.

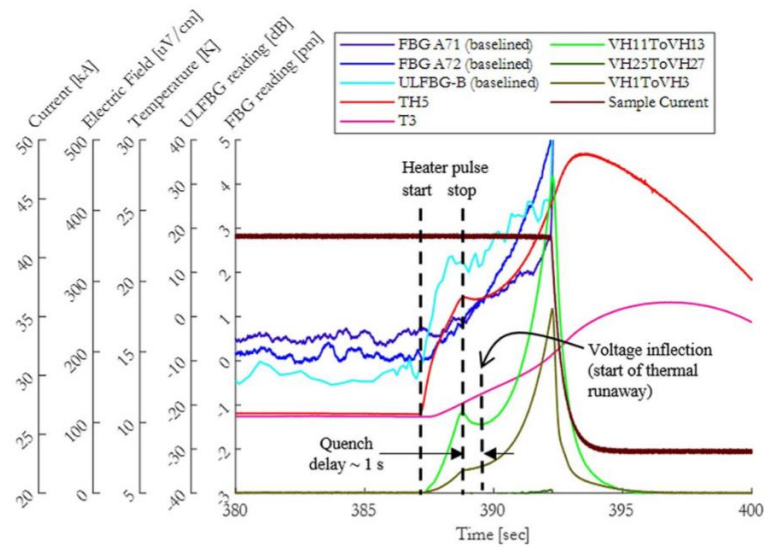


Figure 1.3.4: Result data from the last heat pulse at 10 K [22]

In particular, the FBGs recorded a smaller temperature increase compared to the ULFBGs, attributed mainly to the need for signal filtering due to the noisy raw signal.

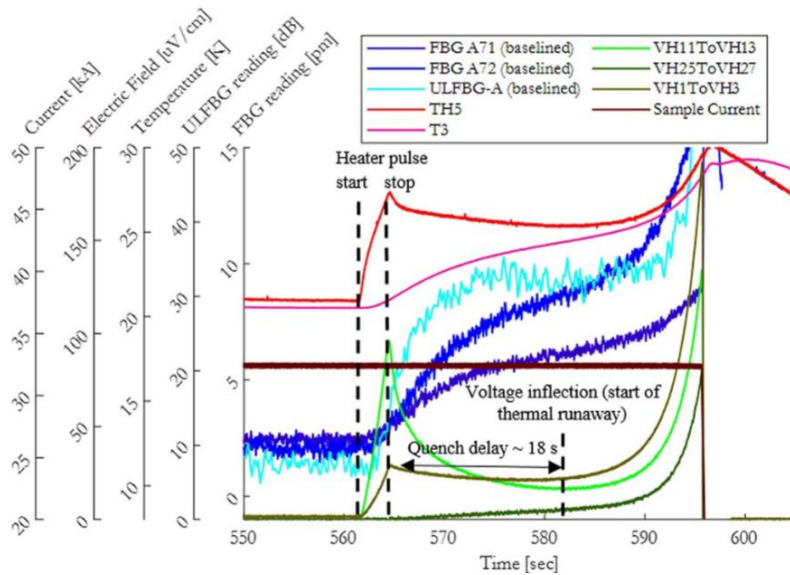


Figure 1.3.5: Result data from the last heat pulse at 20 K [22]

Regarding the response time of the fibers, both types closely follow the signals from the voltage taps and thermocouples, with the signal from the ULFBGs preceding all other instruments. This is because, in the first approximation, the response time is defined as [22]:

$$\Delta t_{FBG} = \Delta t_{adhesive\ diffusion} + \Delta t_{processing} + \Delta t_{propagation}$$

$$\Delta t_{ULFBG} = \Delta t_{adhesive\ diffusion} + \Delta t_{processing}$$

There is an additional contribution to the FBGs caused by the time required for the propagation of information regarding the temperature increase from the quench local hot spot to the sensor. In contrast, this term does not appear in the ULFBGs, as they are composed of a single band of FBGs. The propagation time is therefore dependent on the distance from the local hot spot and the NZPV, which, as previously mentioned, further depends on the thermophysical properties of the medium and external factors such as heat flux and operating-to-critical current ratio too.

The 'adhesive diffusion' time refers to the delay caused by the thermal contact resistance of the epoxy resin, which depends on the thickness and diffusivity of the adhesive material used. Thus, the operational temperature can influence this parameter.

Additionally, there is a time delay associated with processing the raw data and detecting the temperature rise, which is essential to avoid false positives. To achieve this, it is necessary to implement a threshold for the Signal-to-Noise Ratio (SNR), optimizing it to strike the best balance between accuracy and response time in processing this information.

Another experiment conducted by Lu H. et al. [25] for the EAST HTS current leads quench detection using helium gas at 50 K, distributed optical fibers were implemented alongside the voltage taps. In this case, the optical fibers were embedded in a groove of copper strips to prevent breakage and minimize the impact of electromagnetic forces. They were also used to secure the fibers to the surface with polyimide strips instead of epoxy resin. This choice can affect the response time of the signals due to the different diffusivity of the adhesive material.

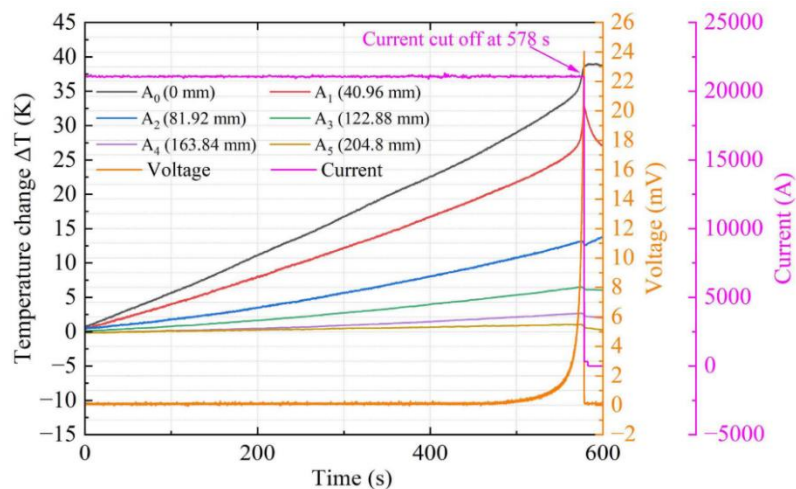


Figure 1.3.6: Results data of the quench event using optical fibers at different positions and voltage taps [25]

As the results show in figures 1.3.5 and 1.3.6, optical fibers can detect the temperature increase signal with high spatial and temporal precision. In this case, the signal from the voltage taps was anticipated by approximately 10 seconds, achieving the lowest possible spatial resolution of just a few millimeters. A significant point to analyze is the vibrations caused by the current cut-off, which could lead to measurement interferences and potentially induce stress on the fibers.

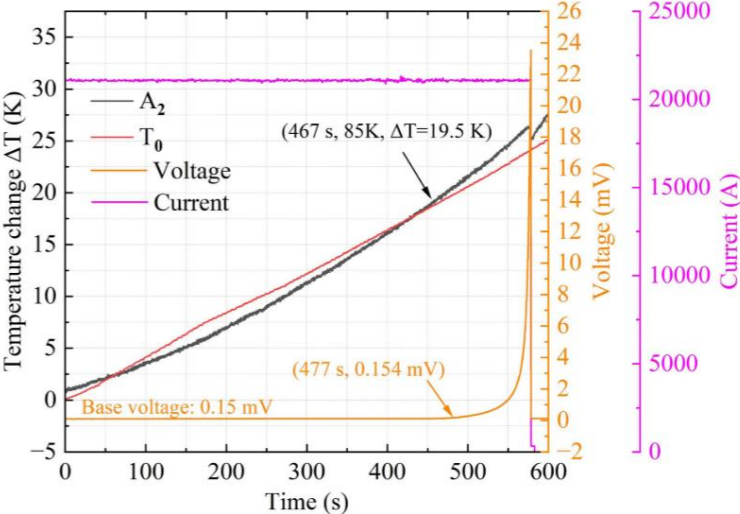


Figure 1.3.7: Difference in time response of the quench detection between optical fiber and voltage taps [25]

At the ENEA Frascati Research Center, researchers are investigating the implementation of optical fibers in a new type of aluminum-core cable with HTS (BSCCO-2223) superconductor for the central solenoid of the EU DEMO fusion reactor [26] [27]. Specifically, an experiment was conducted for quench detection using optical fibers at 77 K in liquid nitrogen flow.

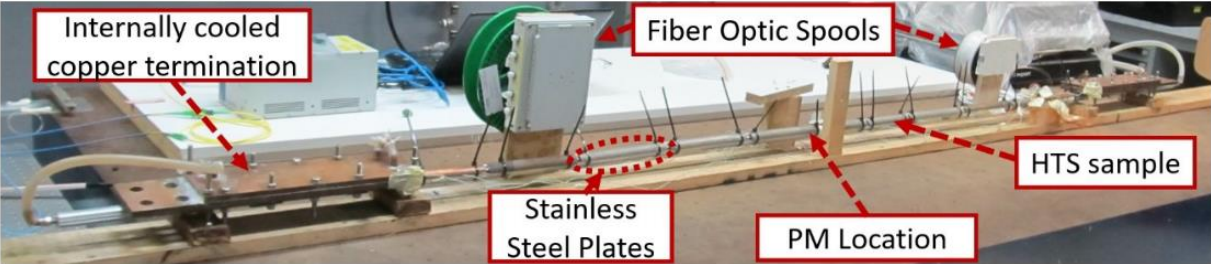


Figure 1.3.8: Setup of the experiment [26]

To induce localized quench by reducing the critical current, a movable permanent magnet was installed at the center of the cable. The optical fibers were positioned above the stack, within the slot of the aluminum core, alongside thermocouples.

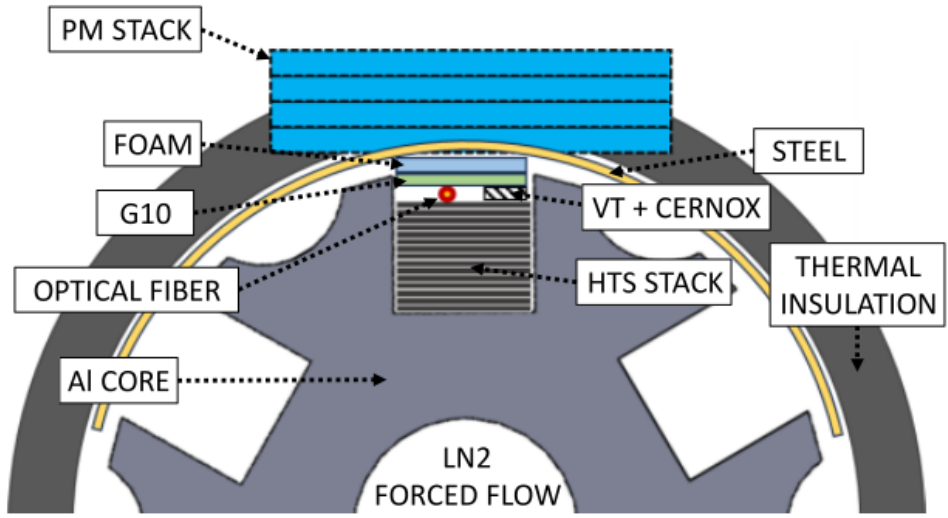


Figure 1.3.9: Section of the cable with the instrumentation installed. The HTS stack is located only in one of the slots [26]

The results here also clearly demonstrate the effectiveness of optical fibers in detecting temperature spikes associated with the transition to the normal zone. Specifically, the slow evolution time of the quench, due to the low NZPV of the HTS, is shown, indicating that quench only occurs at high currents. The slow NZPV is evidenced by the differing temperature trends measured by the thermocouples.

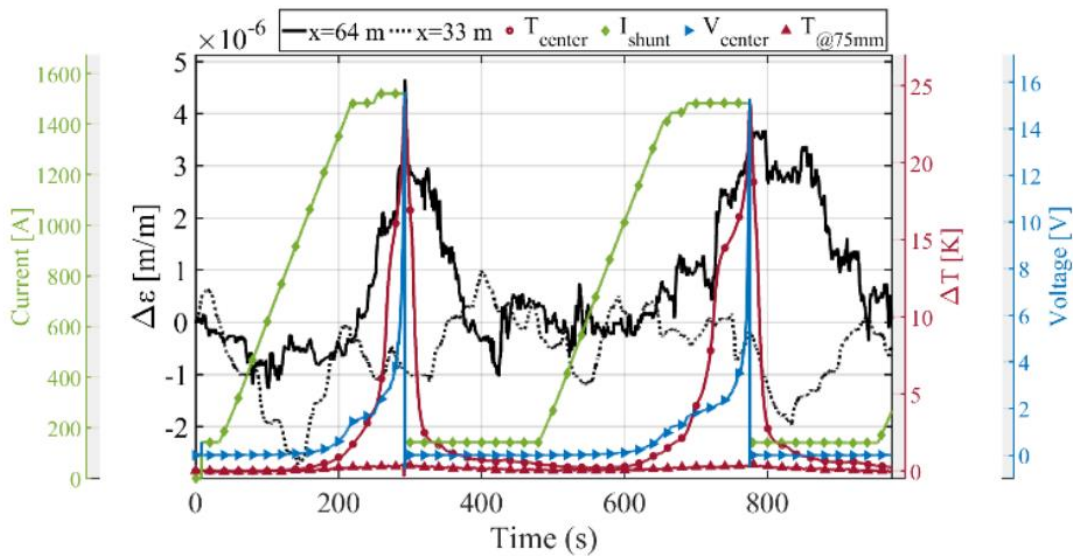


Figure 1.3.10: Results of the quench induced experiment [26]

Furthermore, it was observed that the quench occurred in a very small and highly localized section of the cable, well below the gauge length, the segment of fiber that detects temperature and strain variations. As a result, the temperature distribution along the fiber was not clearly detected and was therefore underestimated.

## 1.4 Aim of the Work

Optical fibers prove to be an excellent tool for quench detection in HTS, being less invasive in terms of volume within cables compared to thermocouples and other instruments. They are immune to external electromagnetic noise and offer a faster quench detection response time. However, several critical points have been identified that require further investigation and solutions, including their fragility and integration into various superconducting cable designs. The objective of this thesis is the exploration and validation of Fiber Bragg Grating (FBG) sensors for quench detection in the high temperature superconducting cables, applying a novel application within a cable-in-conduit design for future magnet systems, embedding FBG sensors in stainless steel capillaries in contact with 10 'Shanghai Superconductor' YBCO tapes [28], within the BRaided STack (BRAST). The description of the aluminum-core cable construction at ENEA Frascati Research Center is presented, with all the process details that has involved, and the instrumentation used for the experiments. The thesis also discusses the results of the FBGs response from quench events in both the liquid nitrogen bath and inflow experiment at 77 K. The objective is not only to demonstrate the feasibility of FBG sensor integration but also to address the technical challenges that come from the construction process and cryogenics operations, such as durability and thermal sensitivity, and the difficulties that arise to compute the NZPV. The results aim to contribute to the development of more reliable superconducting magnet systems for future fusion reactors.

## 2. Sample Preparation and Experimental Setup

A key concept of this experiment is the integration of the BRAFT system within the slotted aluminum core [10]. ENEA has developed several prototypes of Aluminum-slotted core CICC, designed based on tape stacks inserted into helical slots extruded onto an aluminum core, with a reinforced steel or aluminum jacket [29].

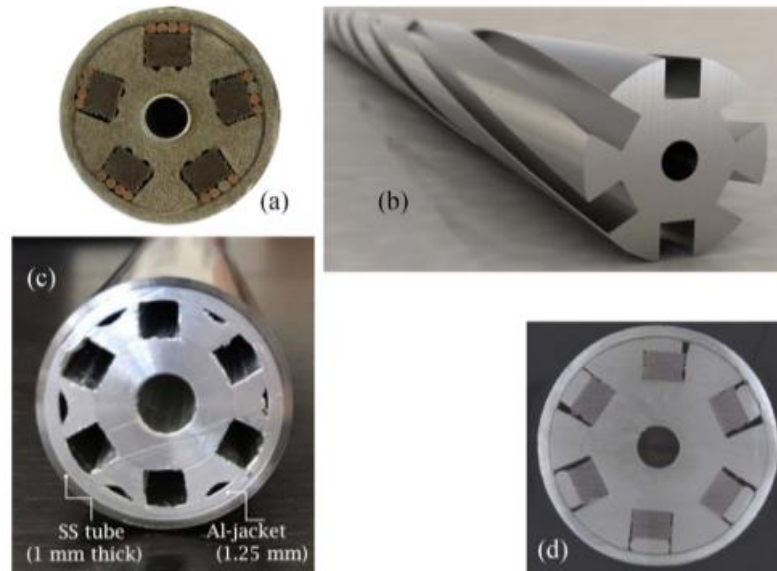


Figure 2.1: Several ENEA Aluminum-slotted CICC: (a) 5-slot cable used for 20kA applications, (b) render of the Aluminum-twisted core cable, (c) and (d) 6-slot core cable [10]

In these cables, the tape stack is left unsoldered within the slots, a choice made due to its proven effectiveness in limiting cable degradation [30], limiting contact between the core stabilizer and the stack, this design reduces thermal and electrical performance. Consequently, a new type of cable, called the SECTOR ASSEMBLED CABLE (SECAS), was developed to meet structural and construction requirements. This design is based on a multi-stage cable structure composed of sub-components, allowing it to minimize AC losses by avoiding a monolithic structure while providing strong mechanical support for the stacks against electromagnetic forces. The ultimate sub-unit concept, known as the BRAIDED STACK (BRAFT), is a design in which the tapes are compacted within a braid of tin-coated copper wires with a diameter of 0.1-0.3 mm. This design makes the cable easier to handle for implementation and provides a flexible structure for handling electromagnetic loads [10]. Additionally, there is the option to insert monitoring instruments, such as optical fibers, through steel capillaries embedded directly within the braid, minimizing fiber exposure and enhancing their protection [31] [32].

A 6-slot aluminum core cable with the BRAFT stack design was thus chosen for implementation.

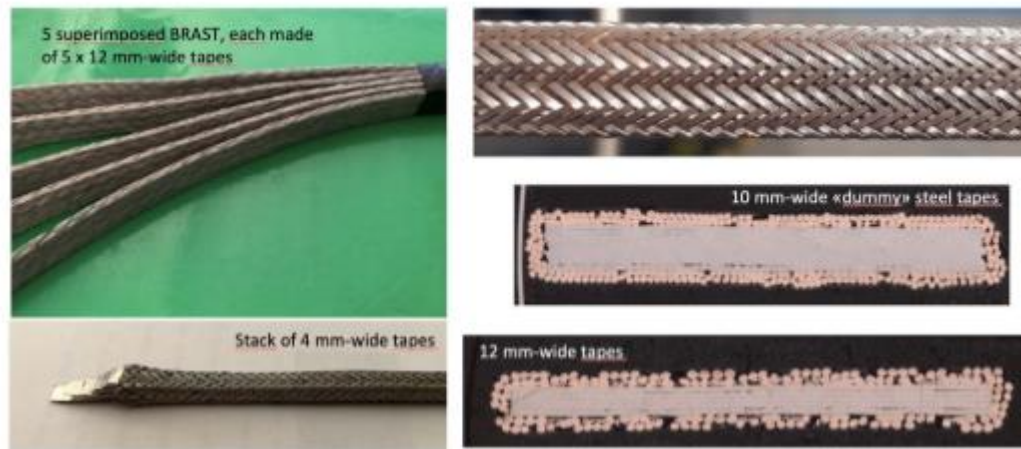


Figure 2.2: Picture of the various kinds of BRAFT stack structure [10]

## 2.1 Sample Cable Preparation

### 2.1.1 Core Preparation

The original core was machined, and the extremities were polished to achieve the pre-determined length for the cable. The core used has the dimensions shown in the table below.

Table 2.1.1: Geometrical parameters of the aluminum core cable

Parameter	Value (mm)
Length $L_{core}$	1000
Diameter $D_{core}$	22.5
Slot width $w_{slot}$	4.5
Slot weight $h_{slot}$	4.1

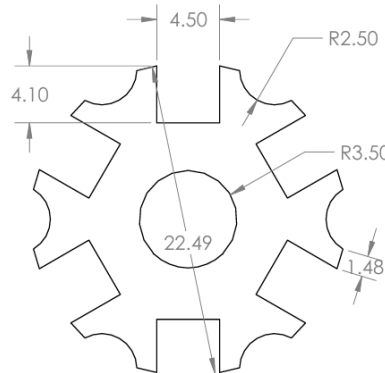


Figure 2.1.1: Sketch of the aluminum 5-slot core section. The measures are reported in millimeters

The slot width matches the width of the 10 tapes used, as previously mentioned, at 4 mm, and provides the space needed to house the BRAST, including the steel capillaries for the fibers. The dimensions of the BRAST used, and a depiction are provided below.

Table 2.1.2: Geometrical parameter of the BRAST used

Parameter	Value (mm)
Width stack $w_s$	0.9
Width braid $w_b$	0.25
Width for capillaries $w_e$	1
Length stack $L_s$	4
Diameter SS capillary $D_{ss,c}$	0.2

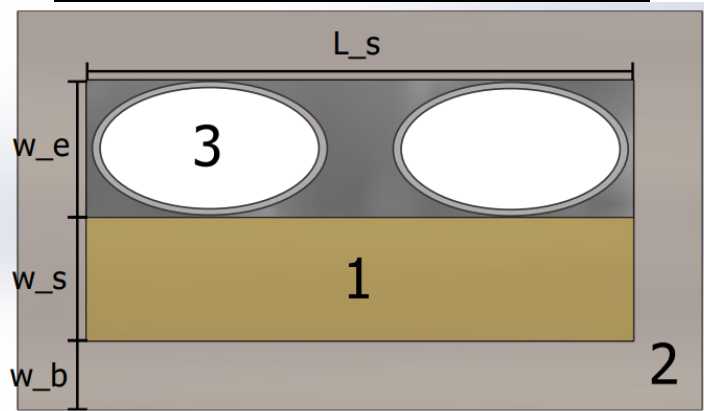


Figure 2.1.2: Sketch of the structure section of the BRAST: the (1) stack is positioned within the (2) braid tin structure and at the bottom of the (3) two steel capillaries

In addition to the optical fibers that will be placed within the steel capillaries, voltage taps have also been implemented at various predefined points along the BRAST. The aluminum core was divided into zones of interest for detecting induced quench. A 'high field' zone was identified at the center of the core, where an external permanent magnet will be placed to locally reduce the critical current. A section extending 100 mm from the cable's center was designated as the high-field zone, with voltage taps spaced 20 mm apart for a total of six taps. This setup is intended to track quench evolution along the cable and potentially identify the NZPV; spatial resolution is essential for observing quench propagation [25] and trade-off was found between the number of voltage taps and the ability to acquire data from the DAQ. Additionally, other voltage taps were placed in predetermined positions to monitor the quench or a potential thermal runaway on the tape: symmetrically to the last voltage tap in the high-field zone, a tap was placed on the opposite side at -100 mm from the center of the cable. Subsequently, two voltage taps were installed symmetrically at the beginning and at the end of the aluminum jacket position. Finally, two voltage taps were placed on the core at the beginning and at the end of the cable, and two at a midpoint between the

start and the end of the cable and the start and the end of the aluminum jacket. The entire arrangement of the voltage tap placements is shown in Figure 2.1.3.

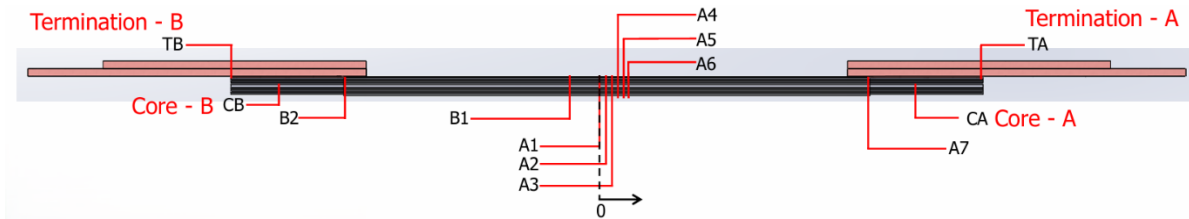


Figure 2.1.3: Sketch of the voltage tap placement on the cable: the high-field zone includes the voltage taps A1-A6, along with the symmetrical B1

This process was quite delicate, particularly for the voltage taps insulating with Kapton tape installed on the lower tape, as it required soldering thin galvanized copper wires with a low-melting-point alloy, which locally altered the structure of the tin braid with a cutting series. The low-melting-point alloy InSn was used to prevent exceeding a temperature of approximately 180°C-200°C during soldering, as temperatures above this range could lead to degradation of the tape [33] [34].



Figure 2.1.4: Picture of the soldering process for the voltage taps in the high-field region on the BRAST

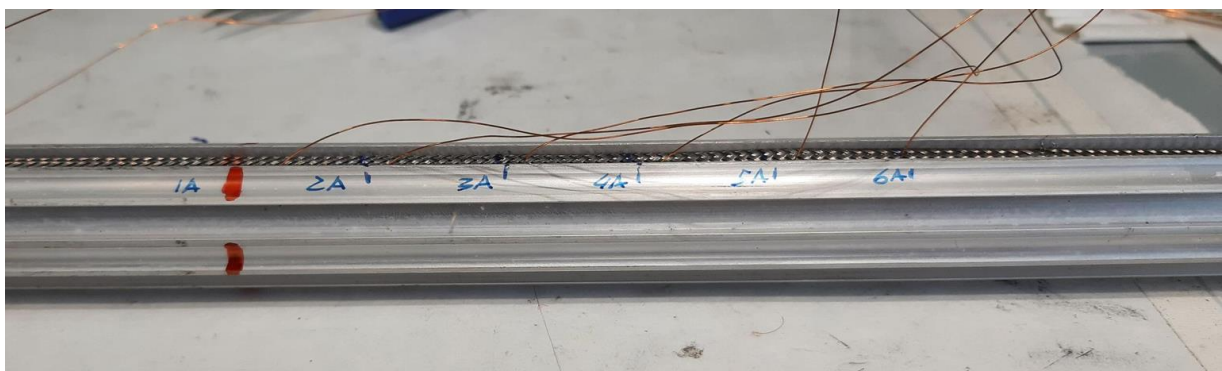
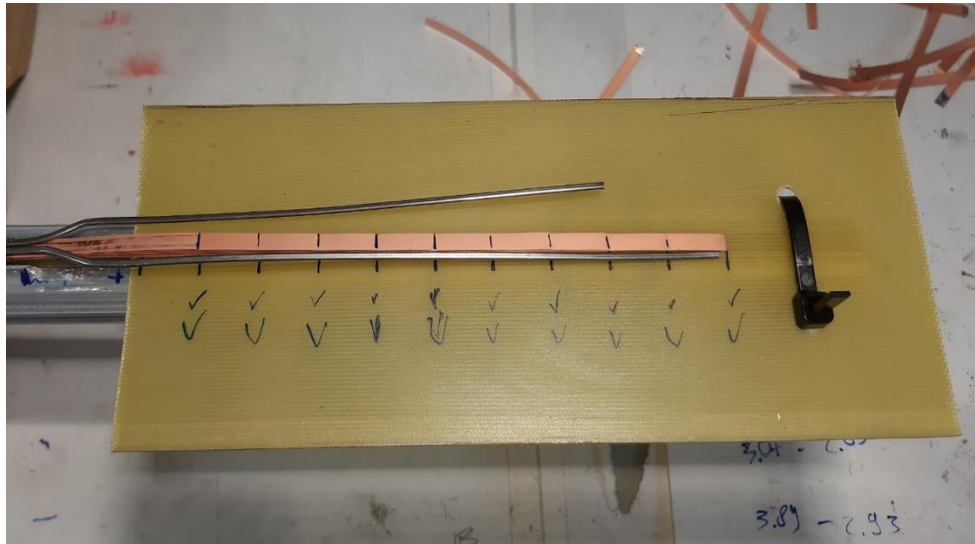


Figure 2.1.5: BRAST integrated into the aluminum core with the voltage taps in the high-field zone

The BRAST tin braid was removed at both ends for a length of 150 mm, leaving the tapes without a containment structure. This was part of the design to allow for subsequent staggering: to distribute current as uniformly as possible across each tape, a staggered arrangement was made from the lowest to the highest tape, with 15 mm increments. This configuration allows a copper rod to be soldered to each section, enabling current to reach each tape.



*Figure 2.1.6: Staggered 15 mm notches on the tapes for pre-soldering.*

Additionally, to address the lack of structure from the braid and electrically isolate the last tape in the stack from the core, a G10 tab was inserted into the slot at each end. To complete the containment structure for the BRAST within the aluminum core, an aluminum filler was designed to be positioned above the BRAST, running along its entire length.

This decision was made to mitigate issues during cooldown due to the difference in thermal expansion coefficients between the aluminum and the components of the BRAST, preventing tape deformation. A rendered model of the cable end configuration is shown in the figure below.

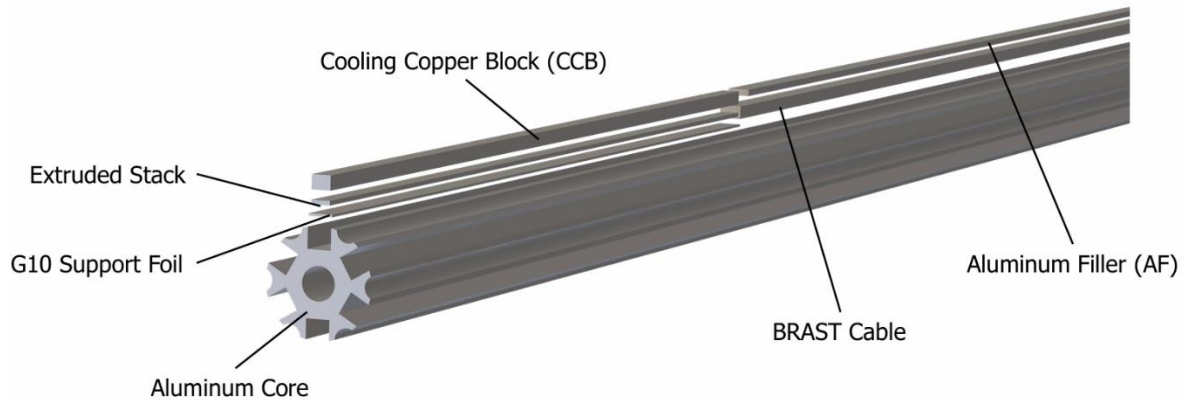


Figure 2.1.7: Rendering of the end portion of the core with its components [35]

Next, the tapes extruded from the braid were pre-soldered with the same low-melting-point alloy InSn to allow them to be soldered to the copper rod. The pre-soldering process required great care due to the mechanical and thermal fragility of the tapes. To improve the adhesion of the solder to the tapes, a flux was applied with absorbent paper to the tapes before each soldering. Once the tapes were pre-soldered, they were soldered to the two copper rods, again using InSn. The result is shown in the figures 2.1.8.

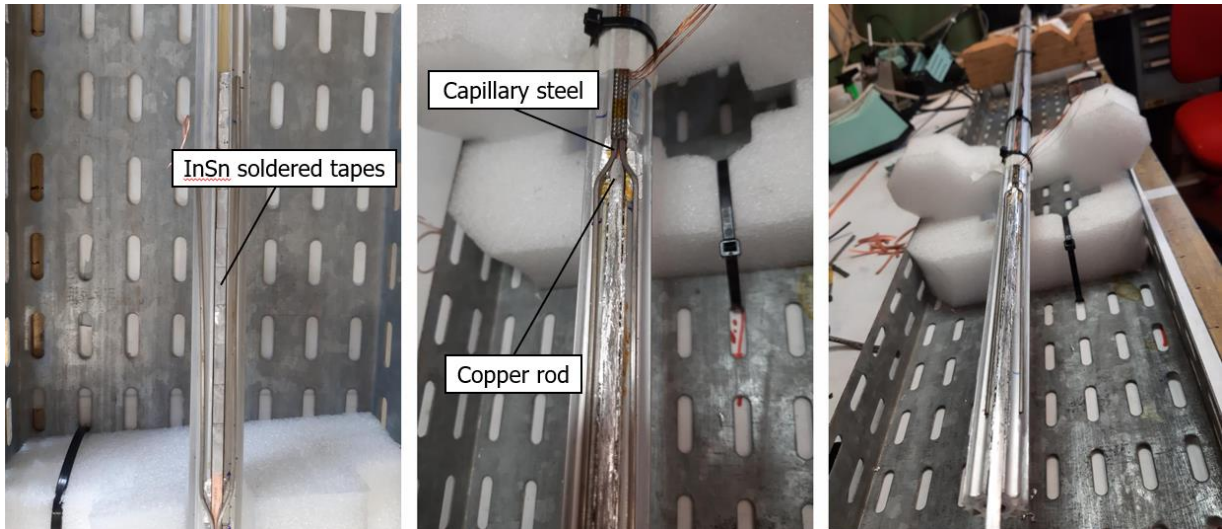


Figure 2.1.8: Final result of the pre-soldering process of the tapes (on the left) and the soldering process with the copper rod (in the center and on the right)

As shown in Figure 2.1.8, particular attention was given to the deviation of the steel capillaries to accommodate the copper rod, which was sharpened to provide a greater holding surface on the tapes and to control the angle of deviation that the fibers inside the capillaries would undergo. It was necessary to soften and round the angles to prevent fractures in the fibers during their installation.

## 2.1.2 Jacketing Process

Afterward, the cable was wrapped in thin layers of stainless steel of approximately 0.2 mm, preparing it for the jacketing process: in this way, the stainless-steel layer ensures the mechanical seal between the stack, the aluminum filler, and the core during the wire-drawing and jacketing process.



*Figure 2.1.9: Wrapped thin layers of stainless steel around the core before the jacketing process*

About the jacket, an aluminum tube with a thickness of 1.32 mm was used for the wire-drawing process, and two brass dies were used, in two different passages, to form the final diameter measure of the cable of 25.20 millimeters. This feature represents an innovation for this type of experiment and cable with respect to the previous experiments [26] [27], aimed at ensuring not only mechanical stability for the stack within the cable but also thermal robustness for the internal optical fibers to detect any temperature variations. In the figure below the method of the jacketing process is presented.



*Figure 2.1.10: Details of the wire-drawing process with one of the brass jigs used*

To ensure the correct jacketing process, a pure isopropanol was used to reduce friction as the figure 2.1.10 shows in the right. The resulting section of the cable with the Aluminum jacket is shown in figure 2.1.11.

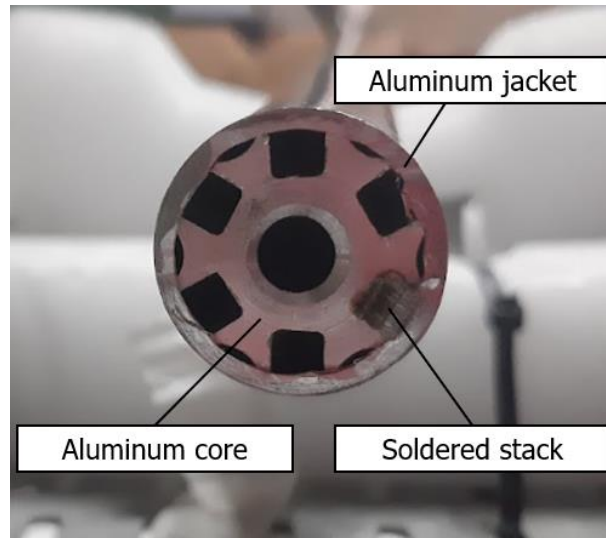


*Figure 2.1.11: Result of the jacketing process*

Following the drawing process, part of the termination section was left exposed, and the copper filler was soldered onto a 3 mm thick copper plate. This plate was then mechanically linked to a pair of terminations, used to cool the cable by flowing liquid nitrogen (LN<sub>2</sub>) [26] [27]. The terminations were fastened together with bolts and secured to the cable on a wooden board, also using bolts. The final setup of the cable is shown in the figure below.

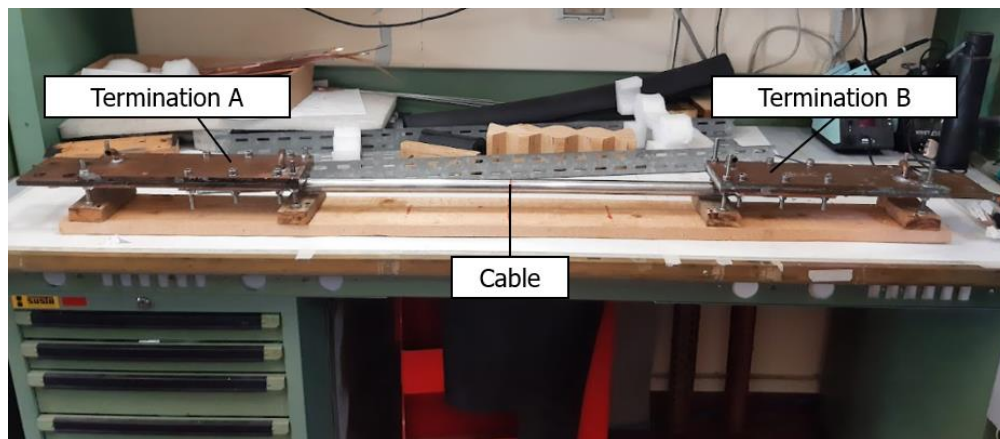


*Figure 2.1.12: Completed sample cable with the copper terminations installed*

### 2.1.3 Optical Fiber Installation

Next, attention was given to installing the optical fibers inside the steel capillaries. Three sets of acrylate-coated optical fibers were used, labeled 504, 505, and 506

according to their serial numbers, as shown in Figure 2.1.13. Two fibers were placed in one capillary and one in the other to investigate the use of multiple fibers for redundant measurement accuracy. It was concluded that for this type of capillary, manually installing more than two optical fibers in the same capillary proves to be quite challenging.

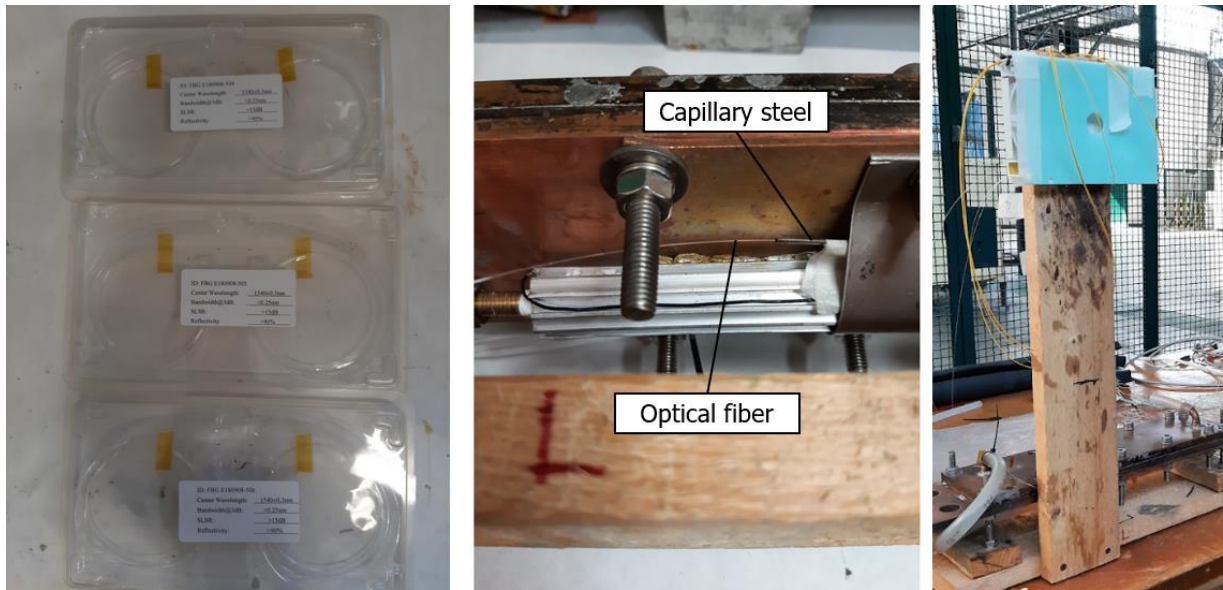


Figure 2.1.13: Fiber Bragg Grating optical fiber used (on the left) and a detail of the optical fiber within the stainless-steel capillary on the center). Structure to house optical fiber in the sample setup on the right)

The manual installation involved threading the fibers into the capillaries while wearing gloves to avoid damage. A vertical wooden block was secured to the board with screws to support the optical fibers and connect them to the interrogator.

Once the cable preparation phase was completed, it was transported to the FATA facility at the ENEA Frascati Research Center to conduct the experiments.

## 2.2 Setup of the Experiments

At the FATA facility, there are five 4 kA power supply units, each responsible for injecting and monitoring current through a torus-based indirect measurement. The power supply units deliver a current bias of approximately 130 A when they turn on. In this setup, the current is measured by capturing the voltage signal induced by the flowing current, using an SCXI-1120 analog-to-digital module [27] [36]. For current data acquisition, a Keithley 2000 [37] multichannel multimeter with a shunt resistor was used. The FBG sensors were monitored with an 8-channel SENTEA DM-8125 interrogator [38]. The instrumentation is monitored from a nearby PC station, as shown in Figure 2.2.1.

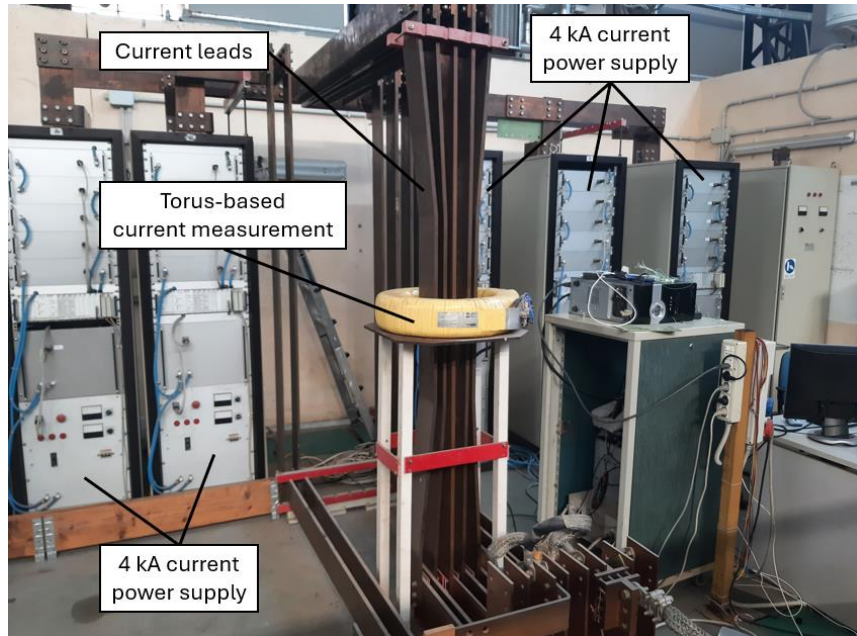


*Figure 2.2.1: Photo of the FATA 20 kA power supply used and the instrumentation station*

For the liquid nitrogen bath setup, a tank was used to hold the cable and its wooden structure. Liquid nitrogen was introduced into the tank at approximately 77 K through a nozzle tube connected to a small pressurized mobile dewar placed nearby. In this setup, it was not possible to recover the cryogenic liquid from the tank after the experiment was completed.

The copper terminations were connected to the 20 kA power supply using bolted braids, positioned to allow isolation from the tank. For the liquid nitrogen flow setup, the nozzle tube from the supply dewar was connected to termination B, while termination A enabled partial recovery of the cryogenic liquid via a secondary empty dewar. A silicon tube was used to connect the terminations and the aluminum core, allowing nitrogen flow into the cable for cooling. CERNOX thermocouples [39] were added to the outer aluminum tube, mounted on a G10 support foil and secured with Kapton tape, to monitor temperature changes on the cable's outer layer.

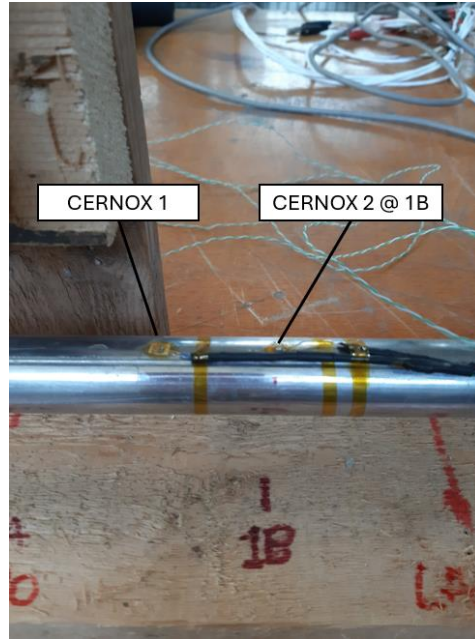


Figure 2.2.2: Details of the CERNOX thermocouples setup on the surface of the aluminum jacket

Additionally, a wooden structure bolted to the base supported a permanent magnet at the cable's center, adjustable in height using a screw above the magnet.

During the latest flow experiments, the two optical fibers inserted in the capillary were replaced with an array of FBGs consisting of 3 optical fibers, each 3 mm wide, spaced 10 mm apart from their center. For the sensitivity mapping of the FBGs, the reference value of 12 pm/K in the 77 K range was used [26]. For the arrays, a different approach was used: the response of the array and the CERNOX thermocouples were analyzed during the heating process from the nominal operating temperature value of about 77 K, as shown in figure 2.2.3.

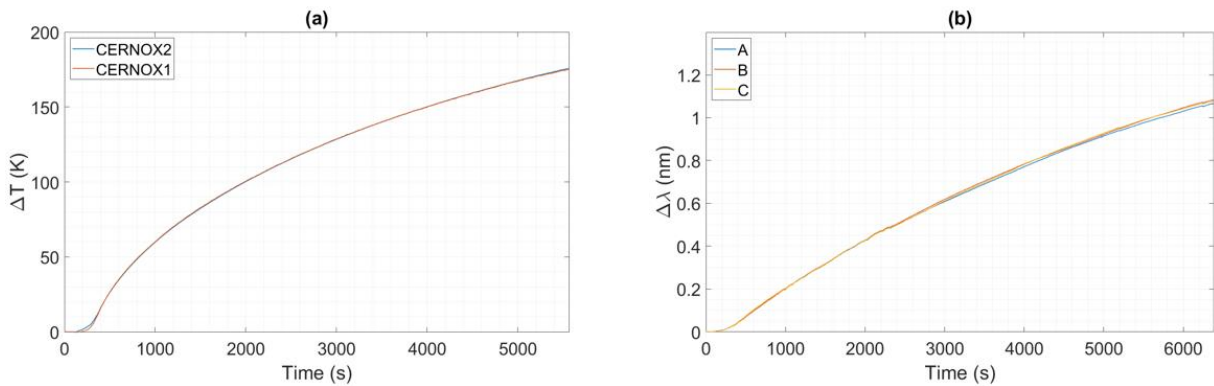
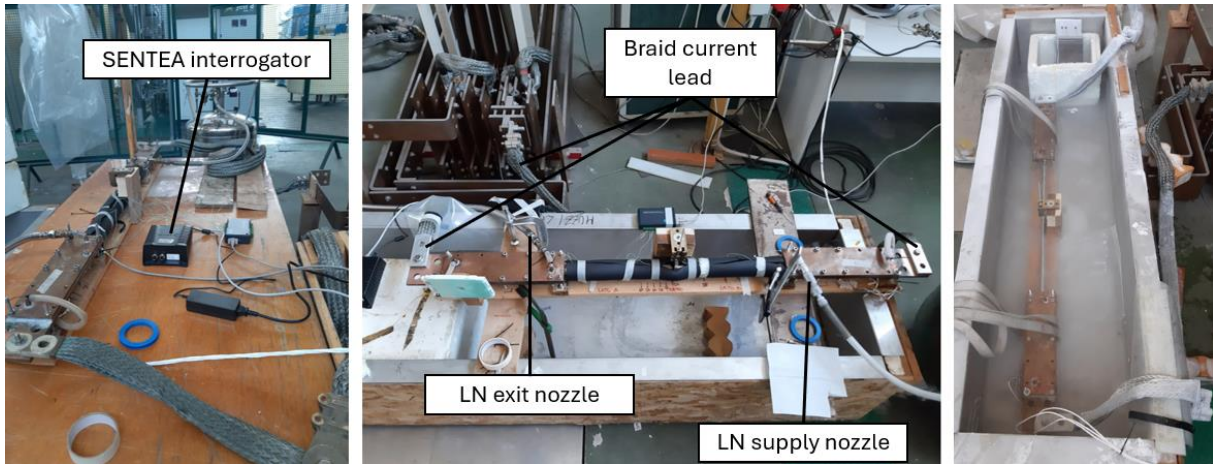


Figure 2.2.3: Response of the CERNOX thermocouples (a) and the FBGs array (b) during the heating transitory to evaluate the sensitivity in terms of relation between  $\Delta\lambda - \Delta T$

To further insulate the cable thermally, an insulating rubber layer was applied over the visible portion of the cable, held in place with insulating tape, exclusively for the flow setup.

To determine the critical currents and n-values, a non-linear fit was performed using the software OriginPRO, applying the power law cited in Chapter 1.



*Figure 2.2.4: Details of the inflow and bath experiment setup*

# 3. Results and Discussion

## 3.1 Test in Liquid Nitrogen Bath at 77 K

Three optical fibers were positioned to detect signals at locations 1A, 1B, and 2B. Additionally, a permanent magnet was placed at the center of the cable, above position 1A. Figures 3.1.1 and 3.1.2 display the recorded voltage signals. In the first figure, a transition is observed in the central portion of the cable where it is disturbed, particularly in the 2A-1A area, as expected. An anomaly, however, was detected in the 2B-1B region, which was undisturbed, suggesting a possible localized defect in that area. A clear change in slope is visible, indicating an increase in resistance.

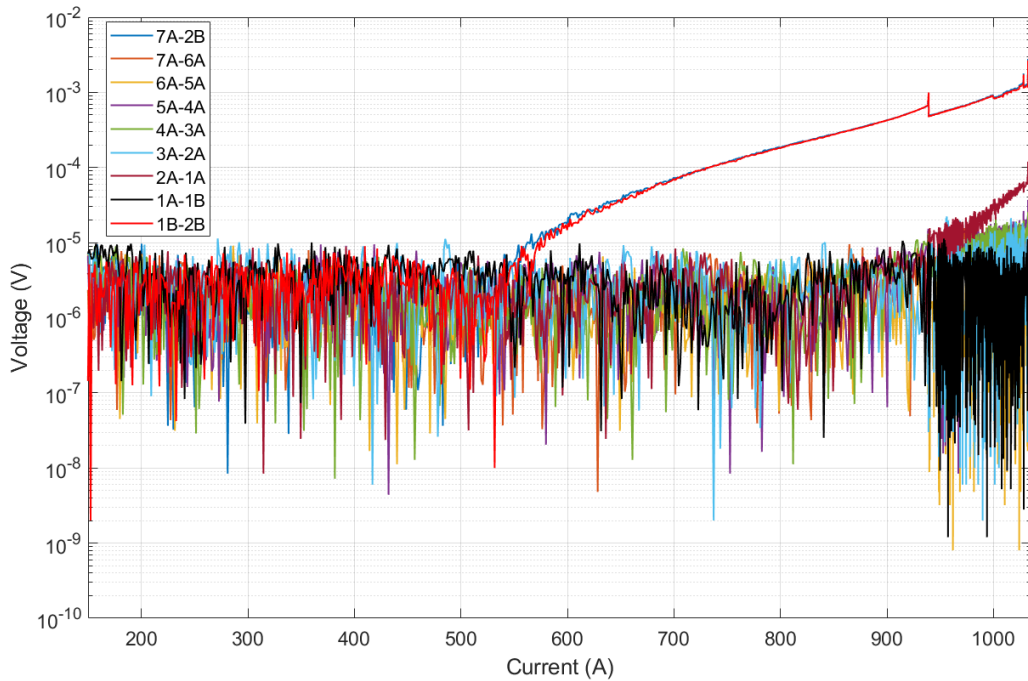


Figure 3.1.1: Voltage signals from the tapes in LN bath

Figure 3.1.2 shows the sections of the cable dedicated to the terminations and the core. It can be observed that a charge transfer is observed at currents where the stack transitions, approximately 550 A, indicating a shift of current towards the resistive elements, such as the core. Since the current flow across the various parallel paths is unknown, it is not straightforward to quantify its value, nor the resistance value, which may vary depending on the length of the section under consideration, making it challenging to interpret directly.

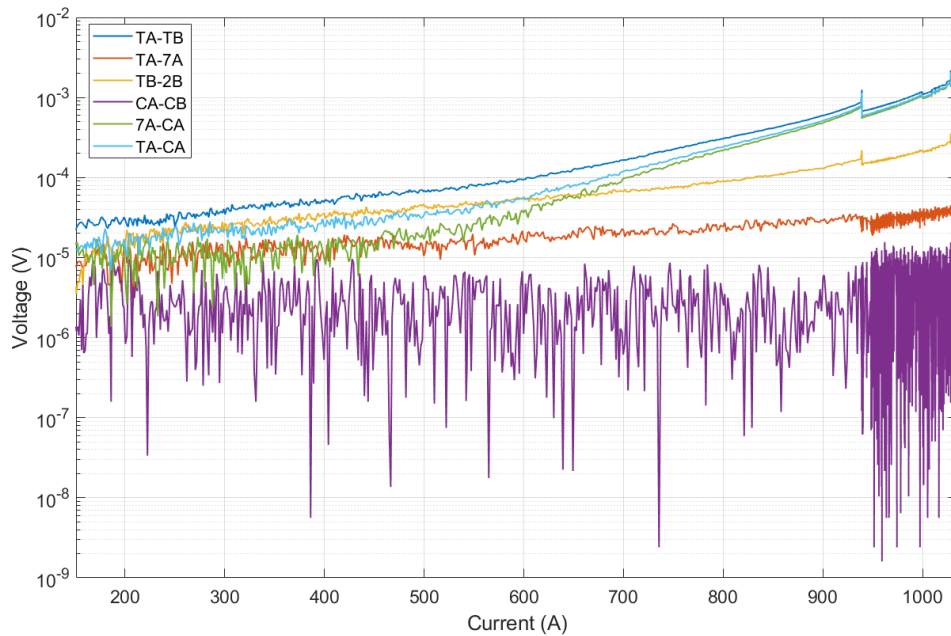


Figure 3.1.2: Voltage signals from the core and terminations in LN bath

Figure 3.1.3 provides a detailed view of the 1B-2B section, particularly illustrating its IV curve in the electric field. As seen in the graph, the critical current is approximately 560 A, with an n-value of 6.3. However, the thermal runaway phenomenon occurs at much higher electric fields and at a current nearly twice the critical current, around 1030 A, indicating a strong stability.

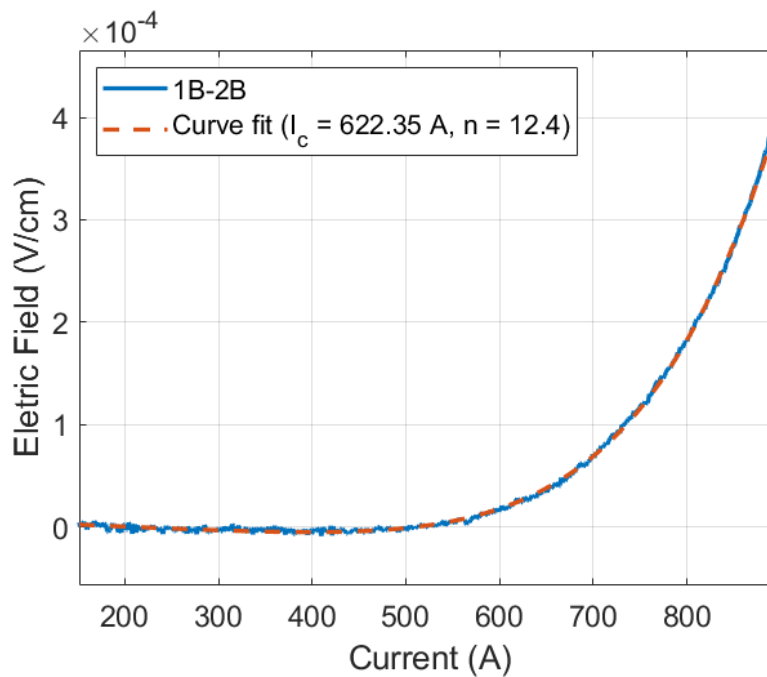


Figure 3.1.3: IV curve of 1B-2B with curve fit in LN bath

In Figure 3.1.4, the central portion of the cable, corresponding to the high magnetic field area on tapes 2A-1A, shows the results of the same fitting process. A critical current of approximately 900 A was obtained, which aligns with the expected value, along with an n-value of 24.3.

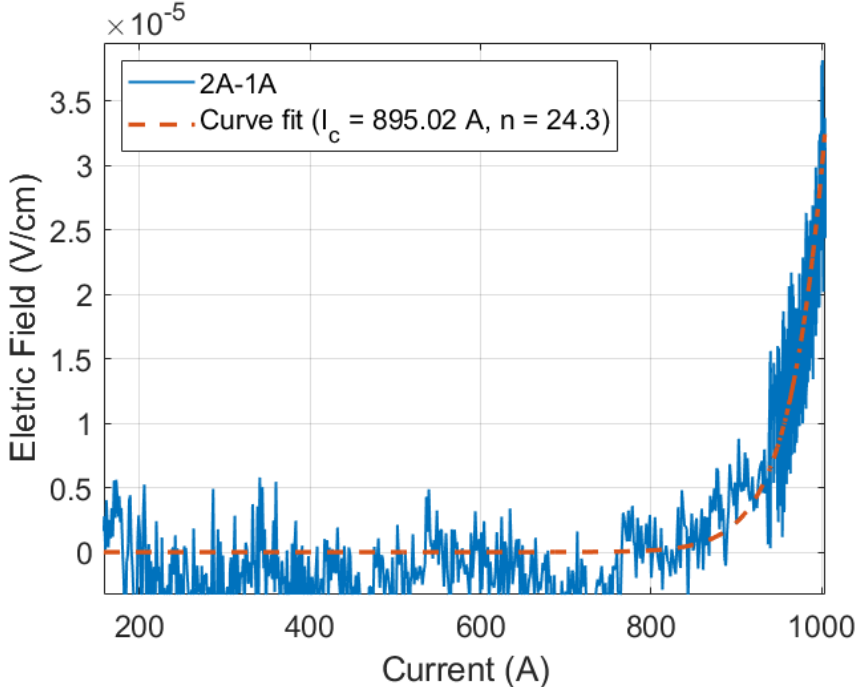


Figure 3.1.4: IV curve of 2A-1A with curve fit in LN bath

Figure 3.1.5 illustrates the moment when the quench phenomenon occurs, showing the response of the voltage taps in the 1B-2B section as well as the FBG sensors located at positions 1A, 1B, and 2B. As can be observed, all three FBGs display a clear response to the event at three different time points. Considering the FBG sensitivity of approximately 12 pm/K in the 77 K range [26], the thermal excursion was in the order of several tens of K, occurring over a very short time span.

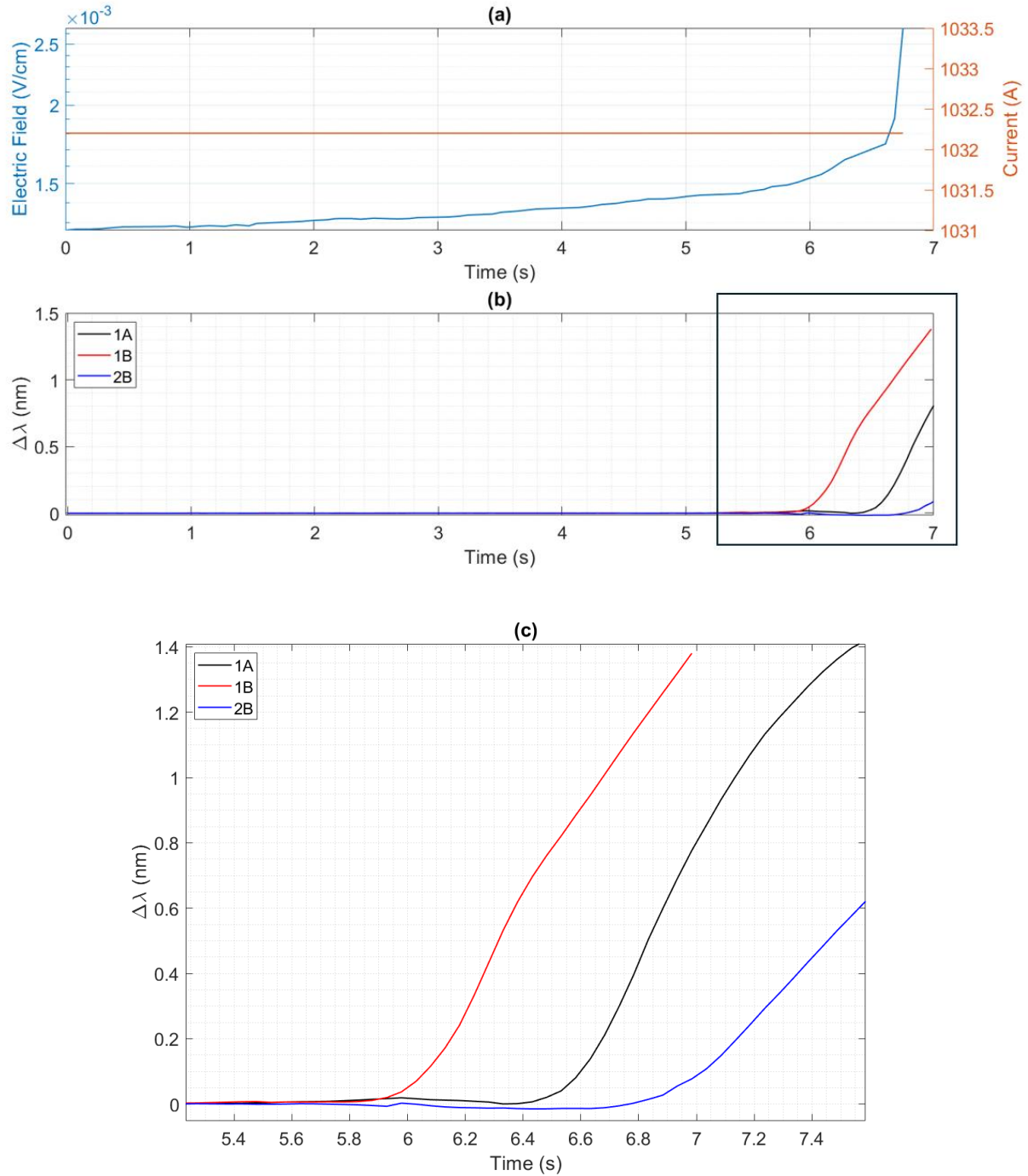


Figure 3.1.5: The response of voltage taps (a) and FBGs (b) in LN bath. (c) Detail of the FBGs response

Without knowing the exact location of the hot spot, it is difficult to draw conclusions about the NZPV. The fact that the FBG positioned at 1B was the first to detect a temperature increase, followed by the FBGs at points 1A and 2B, suggests that the defect may be in the neighborhood of 1B.

This experiment demonstrated the capability of the FBG sensors installed within the steel capillaries to accurately measure temperature variations in the stack.

## 3.2 Test in Liquid Nitrogen Flow at 77 K

To understand better the behavior of the FBGs response during a quench and to verify the capability of temperature minor variations, another experiment with a different approach it was performed: the cable was cooled by liquid nitrogen at 77 K through the inner central channel, similarly to the previous experiment conducted [26] [27]. In figure 3.2.1, the cooling transitory of the cable detected by the 2 CERNOX thermocouples installed, in position 2B and 1B, is presented.

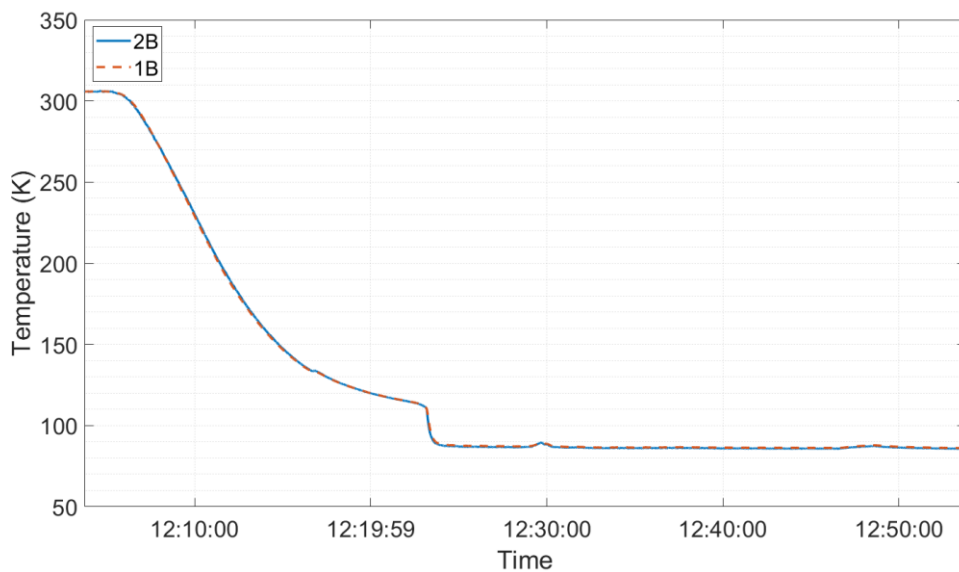


Figure 3.2.1: Cooling transitory measured from the CERNOX thermocouples on the aluminum jacket surface

The graph shows the temperature recorded by thermocouples positioned on the exterior of the aluminum jacket surface, resulting in a few degrees discrepancy from the bulk liquid nitrogen temperature within the central channel. Initially, at the dewar's exit nozzle, the liquid nitrogen instantly evaporates due to the temperature difference between the dewar and the surrounding environment. During the first period of cooling, a two-phase liquid nitrogen flows inside the inner channel. Qualitatively, around 20 minutes after introducing liquid nitrogen into the cable, a sharp temperature drop is observed, attributed to the phase change of the cooler into a complete liquid within the channel at the thermocouple measurement points. In thermal equilibrium, the thermocouples measure a temperature of approximately 85 K.

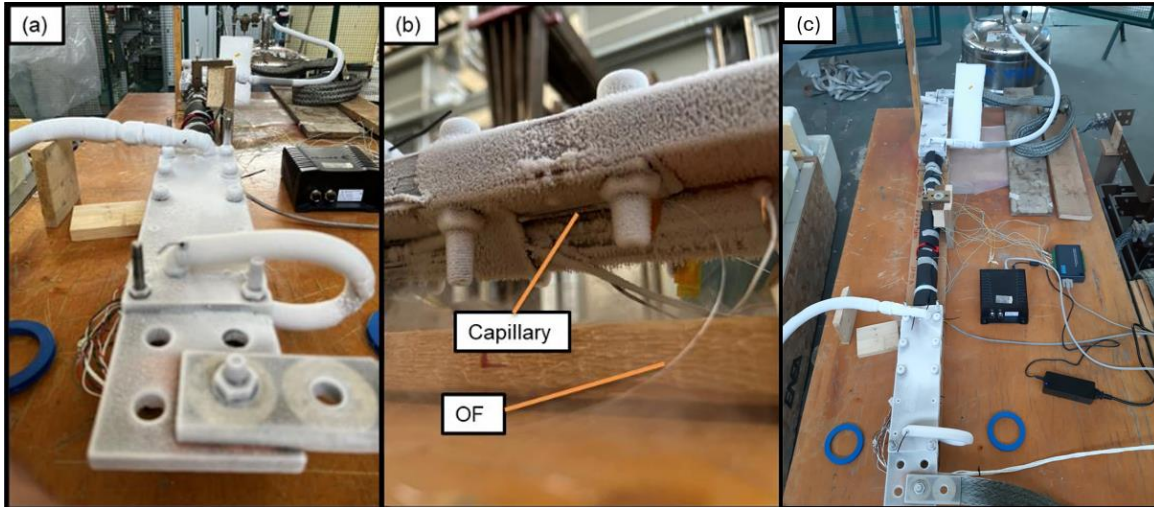


Figure 3.2.2: Pictures of the LN flow setup during the experiment: (a) the detail of the copper termination B, (b) the stainless steel capillary and the optical fiber and (c) upper view of the cable setup [35]

In figure 3.2.3, the voltage signals from the tapes are displayed. As in the bath experiment, this did not affect the optical fiber measurements. A possible explanation for this much earlier transition compared to the previous experiment is that cooling by flow is clearly less effective than bath cooling, making it difficult to dissipate all the thermal power generated by Joule effect on defect. In addition, also the critical current is lower due to the higher temperature related.

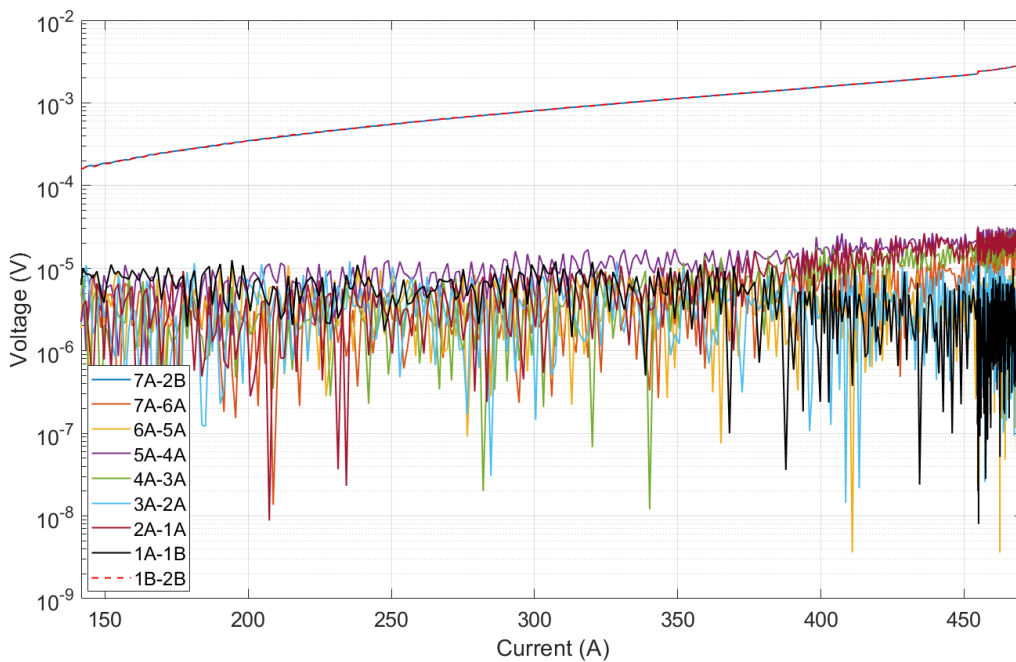


Figure 3.2.3: Voltage signals from the tapes in LN flow

The signals from the core and the terminations show behavior similar to the previous experiment. However, the reduced effectiveness of flow cooling is also evident here, as indicated by the overall increase in resistance values.

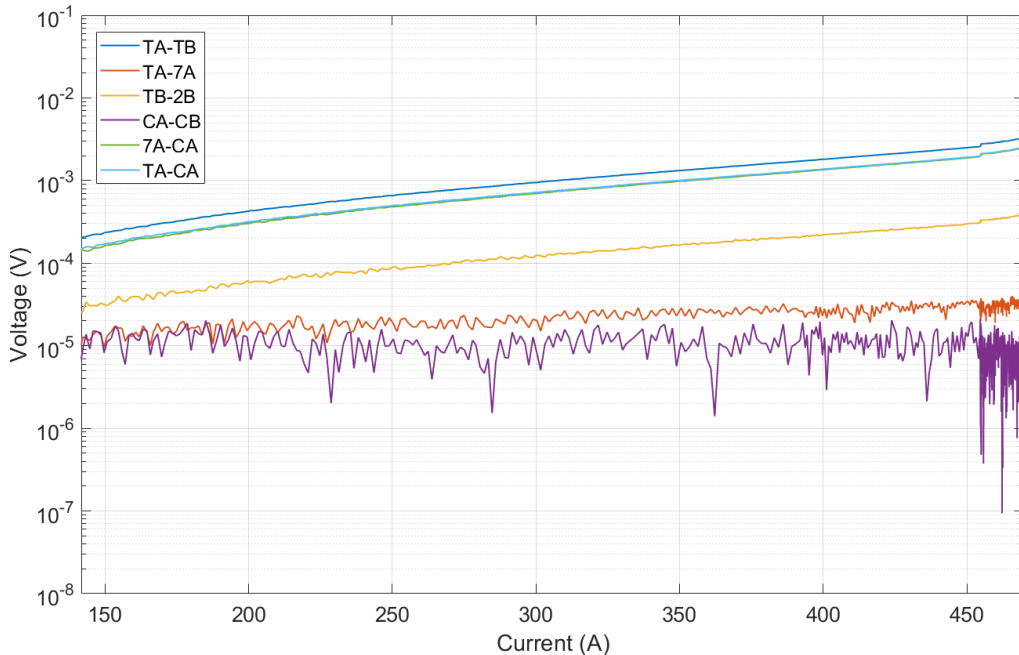


Figure 3.2.4: Voltage signals from the core and terminations in LN flow

Multiple current ramps were performed during each run in order to induce thermal runaways in the stack. As seen in Fig. 3.2.2, the LN2 flow configuration made it possible to manipulate the fibers throughout the experiment: in order to confirm the repeatability across several temperature events, we chose to fix two FBGs in the 2B and 1B positions; to measure the local temperature difference, the third sensor was instead transferred between current ramps in various locations within the cable (designated as the distance from the center later in the text). In the graphs below, results of 3 thermal runaway events are reported.

From the perspective of FBGs 1B and 2B, their response is consistent for all three events: specifically, 2B does not exhibit any appreciable temperature changes, whilst 1B indicates an increase of approximately 1 K compared to the initial run temperature.

The FBG that was moved during the three events is shown in black in the figures below.

The mobile FBG was initially placed in the 2B-1B region, 2 cm from the 1B location, 12 cm from the cable's center, toward termination B. A temperature peak difference of roughly 1 K from FBG at 1B and roughly 2 K from the 2B position is shown in Fig. 3.2.7. Since a temperature rise is detected 12 cm from the center compared to other positions, it can be concluded that the defect is located near this area.

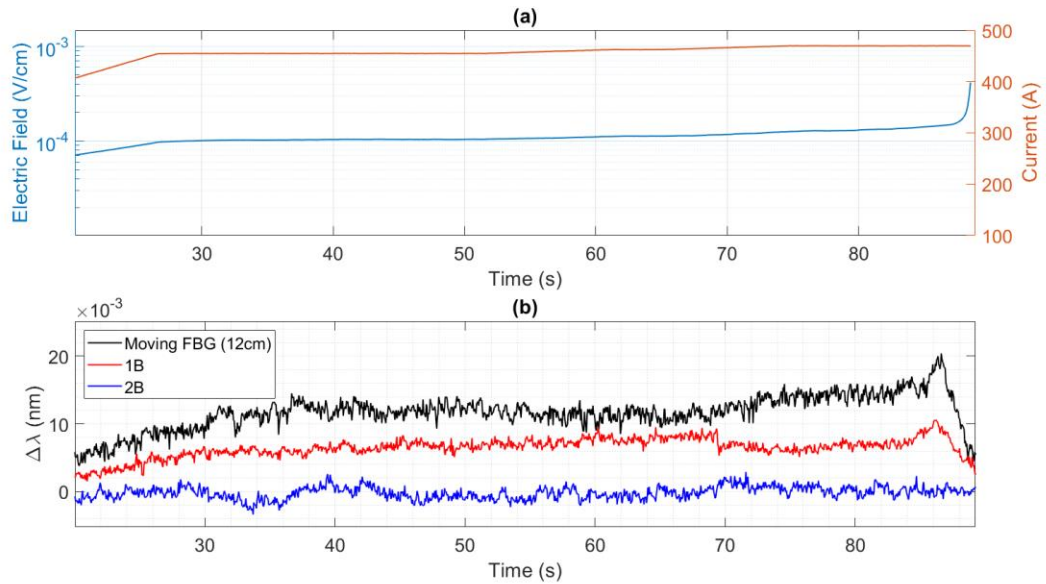


Figure 3.2.5: Detail of the first quench detected, and the response of voltage tap (a) and FBGs (b) in LN flow

The mobile FBG was relocated 2 cm closer to termination B and 14 cm away from the center of the previous run in order to examine better the location of the problem. The outcome was quite similar to the last one, with a temperature difference of almost 3 K from the 1B position and a modest increase in peak temperature of about 4 K above the initial run temperature.

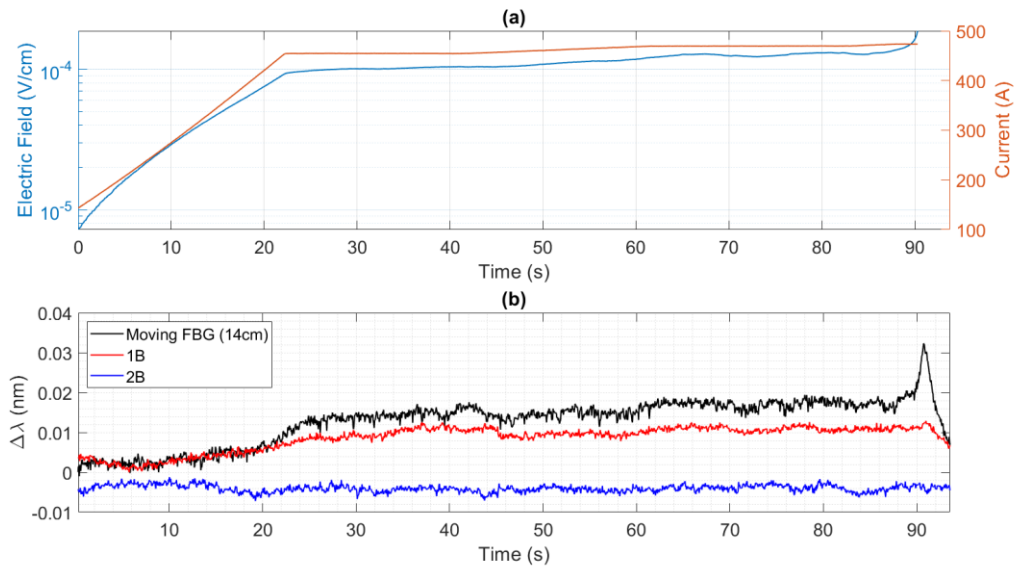


Figure 3.2.6: Detail of the second quench detected, and the response of voltage tap (a) and FBGs (b) in LN flow

The FBG was shifted 13 cm from the cable center, putting it in a central place in relation to the positions of the first two runs, in order to sample the entire surrounding area.

The mobile FBG's temperature increased significantly in this last run, reaching a peak temperature that was roughly 8 K higher than the start of the run and 7 K higher than the temperature at location 1B.

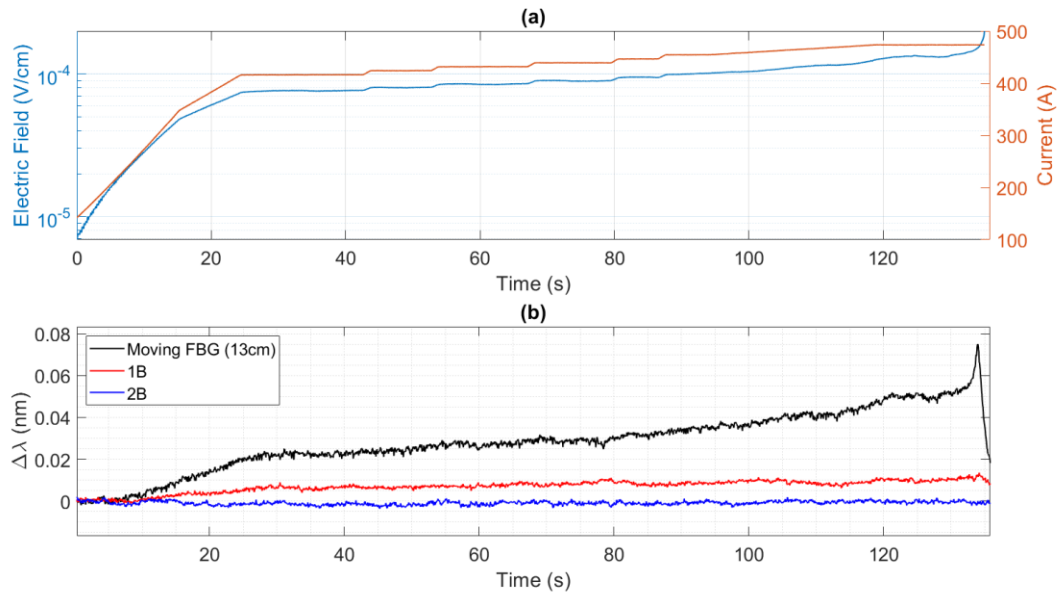


Figure 3.2.7: Detail of the third quench detected, and the response of voltage tap (a) and FBGs (b) in LN flow

The cable stability even under flow cooling circumstances is once again demonstrated by the fact that thermal runaway occurred at the same current and electric field in all three conducted runs, despite the lower currents and fields with respect to the bath experiment.

Throughout the three runs, temperature changes were even observed by the CERNOX thermocouples; the one in position 1B recorded a change of about 0.2 K in all occurrences, which is significantly less than the variations displayed by the FBGs. In contrast to the FBGs, which are in direct contact with the tapes inside the steel capillaries, the thermocouples are externally placed on the aluminum jacket, making their placement and measurement more peripheral.

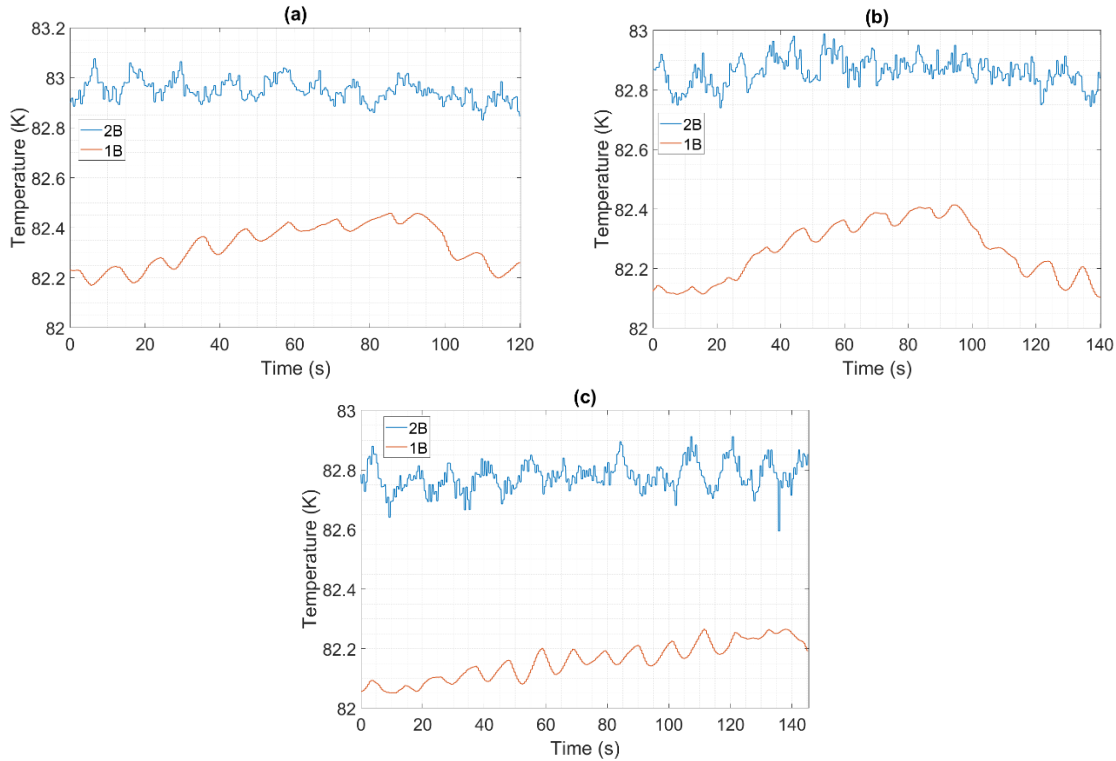


Figure 3.2.8: Temperature acquired by the CERNOX during the first (a), second (b) and third (c) quench events

To confirm the defect location utilizing the optical fibers and to properly evaluate the quench propagation in the sample, more flow experiments were carried out.

An array of different 3 FBG, named A, B and C with a smaller coating cross section, was substituted into one capillary measuring positions as the following figure describes, while the last FBG in the other capillary was monitored the position at 13 cm by the center of the cable.

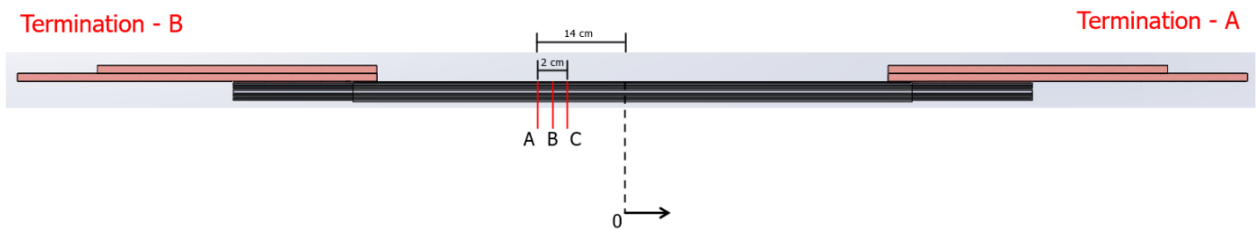


Figure 3.2.9: New configuration for the FBGs array position

The FBGs array was moved toward termination A by 0.5 cm, 1 cm, 2 cm, and 2.5 cm from the starting positions in between each run. During this experiment the quench detection signal experiment was relieved, manually stopping the experiment, in order to achieve higher temperatures inside the cable during the quench event. The quench detection signal threshold also increased to roughly 5E-2 V.

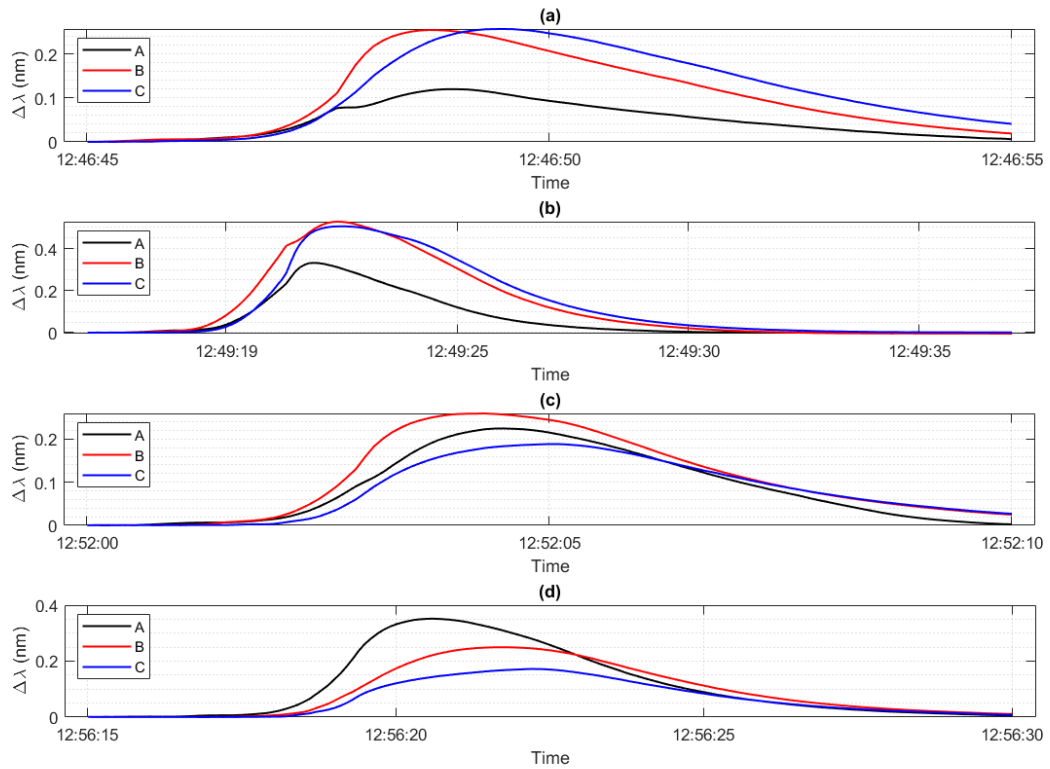


Figure 3.2.10: Different FBGs position for the evaluation of defect location: (a) FBGs array towards +0.5 cm to Termination A, (b) towards +1.0 cm, (c) towards +2.0 cm and (d) towards +2.5 cm

The findings are shown in Figure 3.2.9, where it can be observed that initially sensor B responds first, followed by C and A, suggesting that the defect is located near B. As the array is moved towards termination A, there is an inversion in the sensor response behavior, with sensor A receiving a response before the other two, suggesting that it has approached the defect area where B and C were previously located.

As can be seen in the figure 3.2.10, for the max value found of  $\Delta\lambda \approx 0.5$  nm, in the figure 3.2.9, it corresponds with an increase in temperature of approximately 100 K, confirming the big excursion in temperature in very short time.

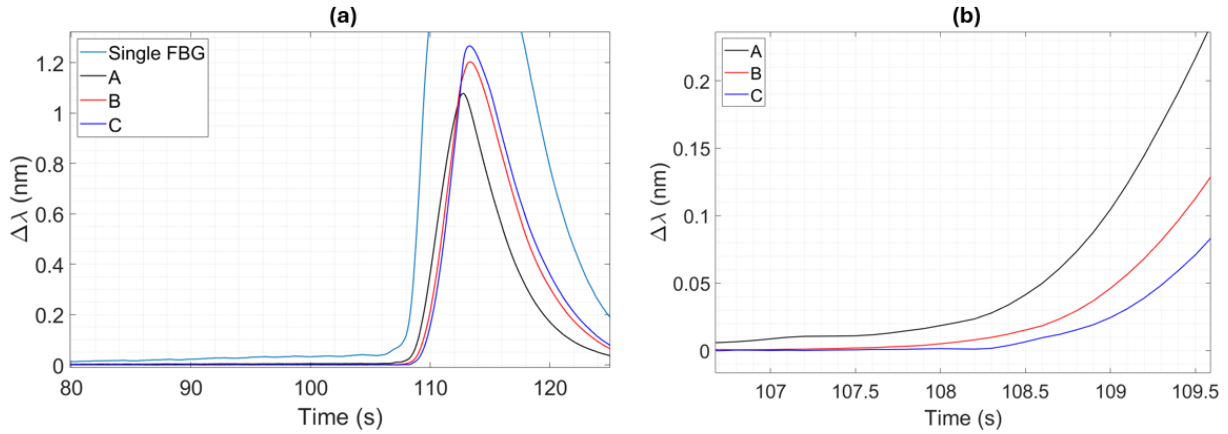


Figure 3.2.11: Response of the FBGs during one of the main quenches: (a) the results of different coating cross-section on sensitivity (the single FBG went off-scale), (b) the detail of the FBG array response during the quench event

In figure 3.2.11, one of the main thermal runaways of all optical fibers deployed on the new positions, with an offset of approximately 2.5 cm, is displayed. It is evident that the Bragg wavelength measurement of the FBGs array differs from that of the single FBG with the larger coating section. This disparity results from coating cross-section's influence on the strain response  $\varepsilon$ . Specifically, the single FBG measurement went off-scale, as shown in the figure.

The order of the peaks captured by the FBGs (left) and the beginning of thermal runaway, which is measured by the same FBGs (right), gives an indication of the heat propagation along the cable.

Calculating the NZPV with voltage taps, in this case, is not straightforward as the exact hotspot location is not well-defined. So, the analysis of the NZPV with the FBGs array is performed. Two measurements with the same current ramp and same conditions are considered for the evaluation of the NZPV.

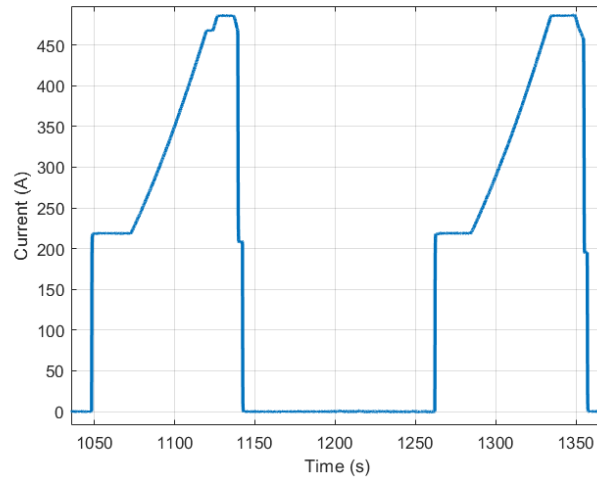


Figure 3.2.12: Current rump of the two experiments run for the NZPV computation

The NZPV can be roughly expressed as the ratio between the difference in distance between two sensors and the time it takes for the normal zone to spread across the same distance [21] [40]:

$$NZPV \approx \frac{\Delta x_{FBG}}{t_{prop,2} - t_{prop,1}}$$

Equation 3.2.1

As a reference to the propagation time in the FBG sensors, the moment when the first derivative of the temperature measurement shows a sharp change can be used.

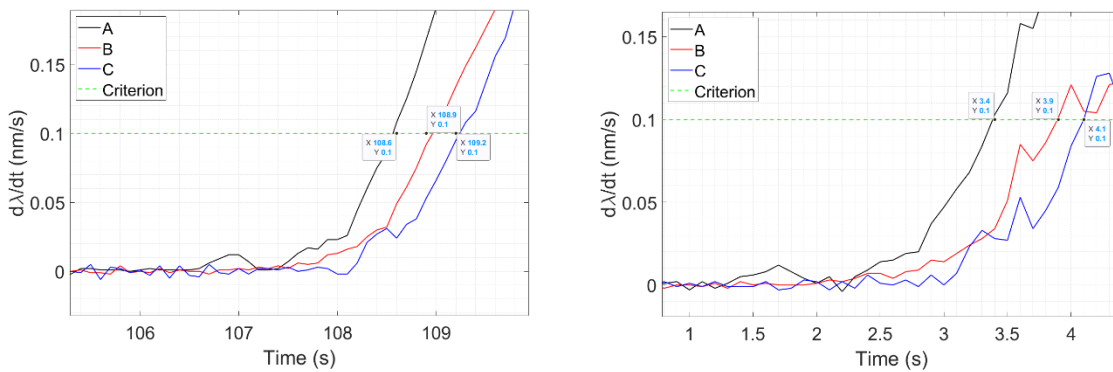


Figure 3.2.13: Time derivative of the FBGs signals: the points highlighted represent the time in which the signal slope increases and starts the thermal runaway

Table 3.2.1: Results derived from the NZPV calculation

Zone	$\Delta x$ (cm)	$\Delta t$ (s)	NZPV(cm/s)
First measure A-B	1.0	0.4	2.5
First measure B-C	1.0	0.2	5.0
First measure A-C	2.0	0.6	3.3

Second measure A-B	1.0	0.5	2.0
Second measure B-C	1.0	0.2	5.0
Second Measure A-C	2.0	0.7	2.9

In table 3.2.1 the values of the NZPV obtained are reported. As observed, in both events the NZPV remains relatively constant, ranging between 2.0 cm/s and 5.0 cm/s, with a mean NZPV approximately of 3.0 cm/s, aligning with the predictions for HTS and, in particular, for the REBCO tapes [41] [42]. It is necessary to take into accounts a certain relative error of approximately 10% associated with the measurement of the FBGs array position. This uncertainty arises primarily from inaccuracies in positioning during the initial setup and from variations introduced when moving the optical fibers between measurement runs. To improve the accuracy of measurements and better understand the factors influencing the NZPV computation, it would be beneficial to consider a dedicated experimental setup, aiming to measure the NZPV while minimizing the disturbance errors. An approach could involve the integration of resistance measurements [43]. Moreover, the development of a numerical model could provide a robust framework for simulating the quench dynamics [44].

Future work should also investigate the potential of fully automated systems to reduce human-induced variability. Additionally, an in-depth study of the mechanical and thermal interactions between the optical fibers and the superconducting cable could further refine the positioning accuracy and enhance the overall measurement reliability: these advancements would contribute to a more precise characterization of the NZPV measurement.

## 4. Conclusion and Perspectives

In this work, an experimental study was conducted on the effectiveness in detecting quench events of FBG optical sensors integrated in a superconducting cable for fusion applications.

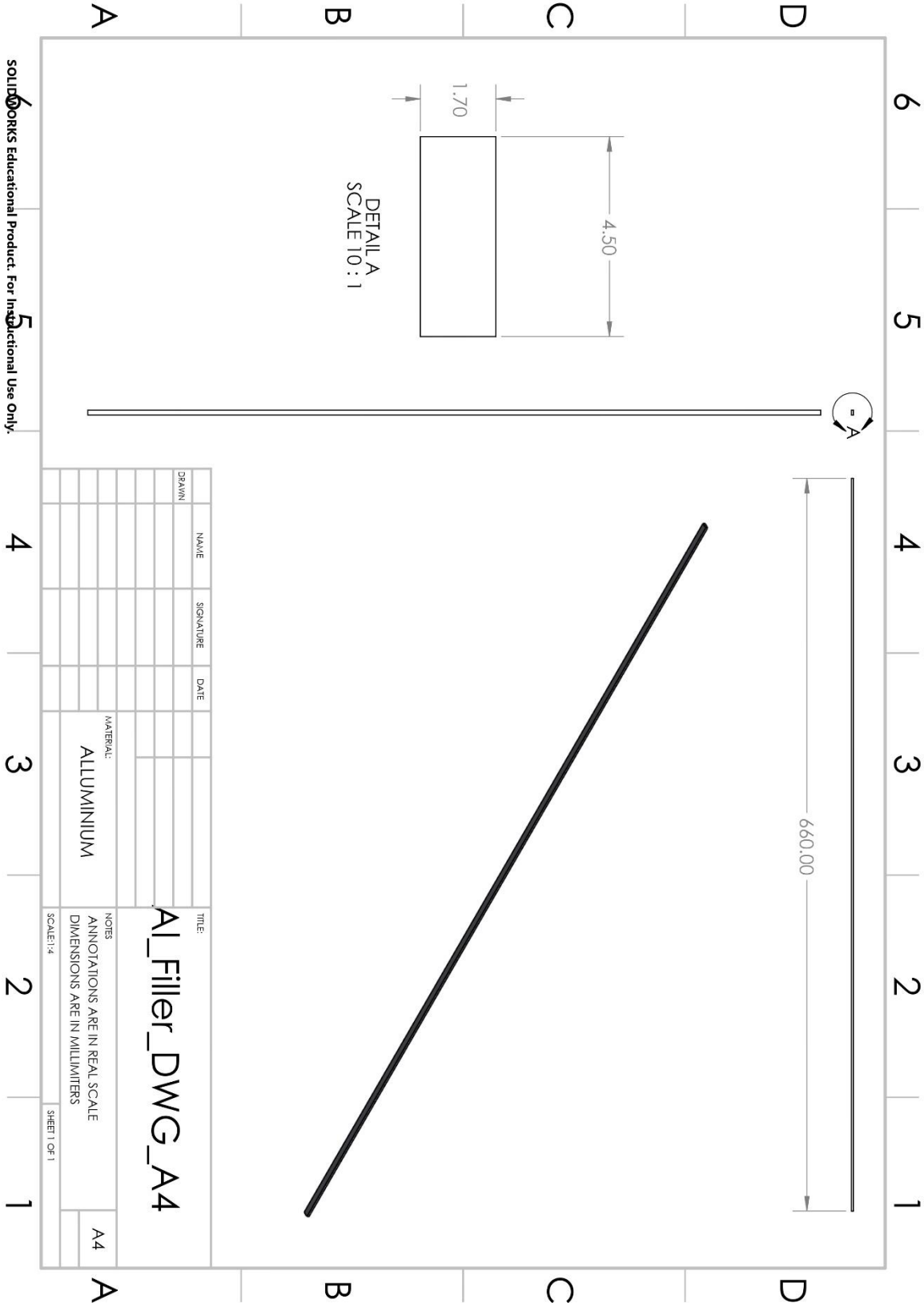
The design of the sample is included in the experimental section, describing the manufacturing process carried out in this thesis. A 6-slotted core aluminum sample cable design was adopted by exploiting two steel capillaries inside a BRAided STack (BRAST) for the insertion of optical fibers in close contact with the superconducting elements.

Different experiments in liquid nitrogen bath and liquid nitrogen flow at 77 K were conducted. The results demonstrated that the response of the optical sensors to temperature variations following quench events and thermal runaways aligned with the response from the voltage taps installed at the same locations, validating the use of this method for quench detection. The optical sensors response is furthermore higher with respect to conventional thermometers placed on the cable jackets in evaluating thermal excursions in case of a quench.

The results collected furthermore allow to evaluate a crucial parameter for such systems, the NZPV, yielding the mean values of 3.0 cm/s. These results align with the expected values for HTS compounds. To the best of my knowledge, the measurement of the NZPV through optical fibers in HTS-based cables represents a novelty.

In conclusion, the work carried out in this thesis allow to affirm that FBG optical fibers may represent a solution for quench detection, offering several advantages with respect to traditional voltage methods, such as being less invasive in terms of volume within cables compared to thermocouples and other instruments, immunity to external electromagnetic noise, and fast quench detection response time.

# Appendix A – Drawings of the Cable Design

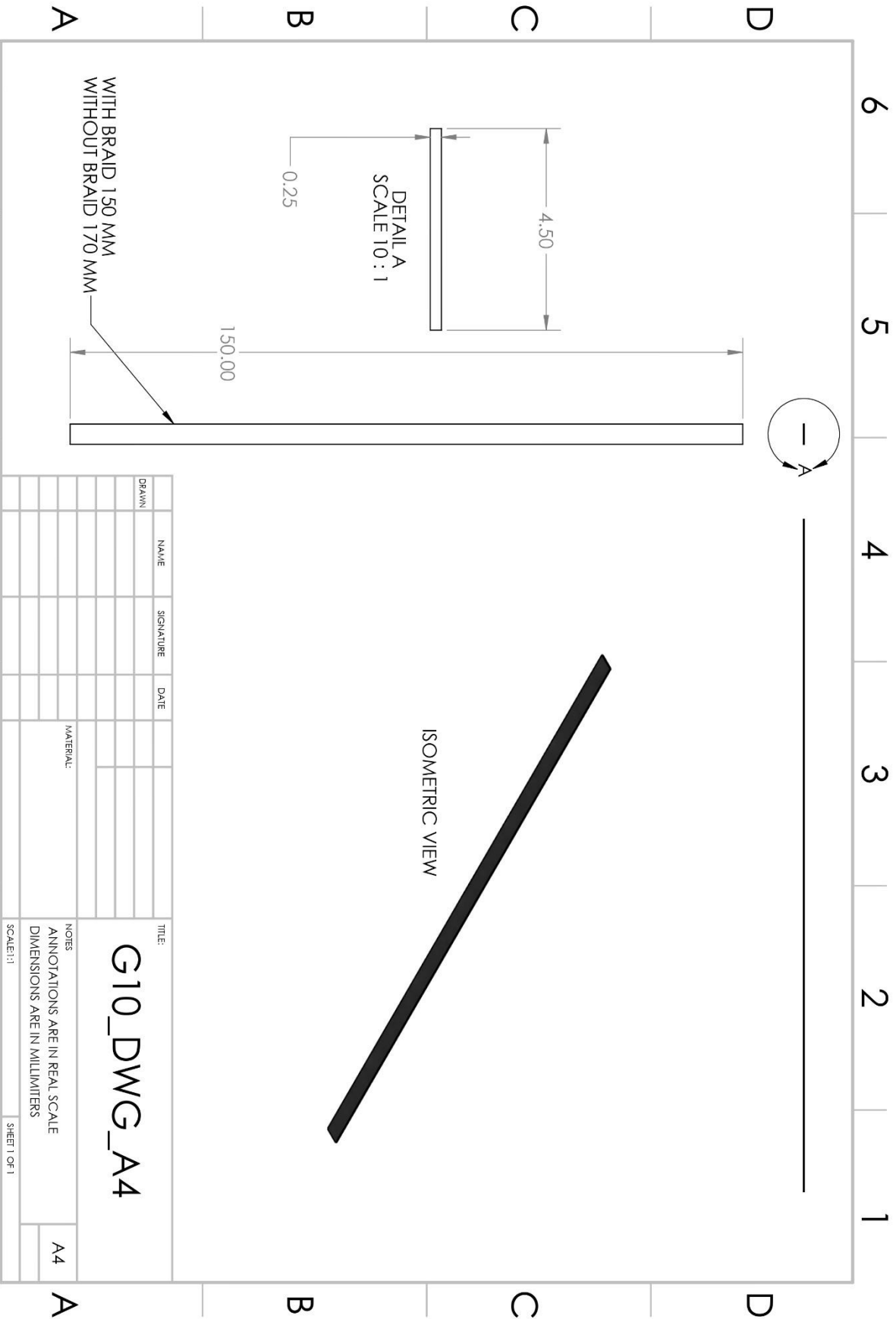


SOLIDWORKS Educational Product. For Instructional Use Only.

DRAWN	NAME	SIGNATURE	DATE	TITLE
				<b>Al_Filler_DWG_A4</b>
				NOTES
				ANNOTATIONS ARE IN REAL SCALE
				DIMENSIONS ARE IN MILLIMETERS
				SCALE: 1:4
				SHEET 1 OF 1
				MATERIAL:
				ALUMINIUM
				A4

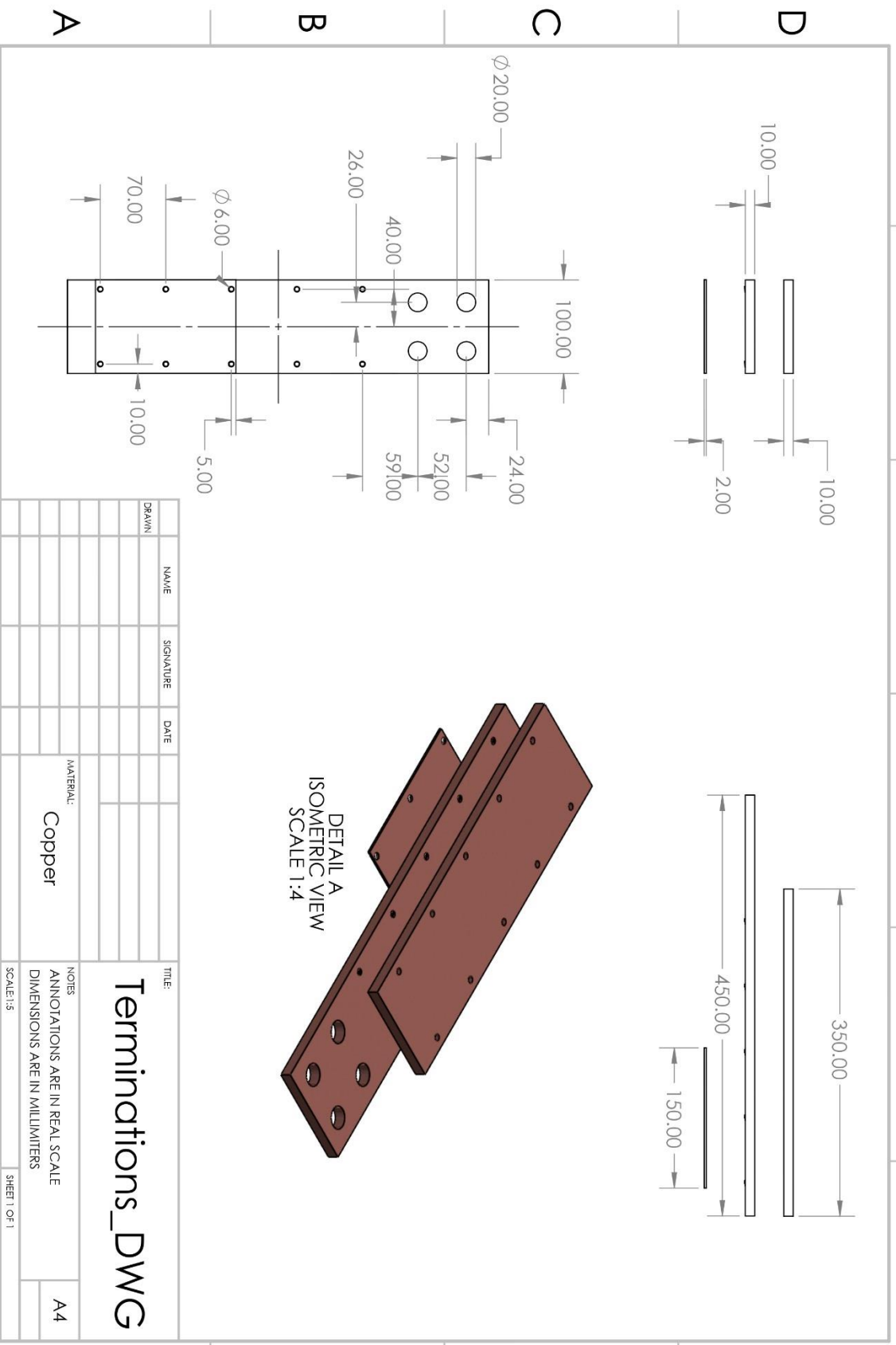






SOLIDWORKS Educational Product. For Instructional Use Only.

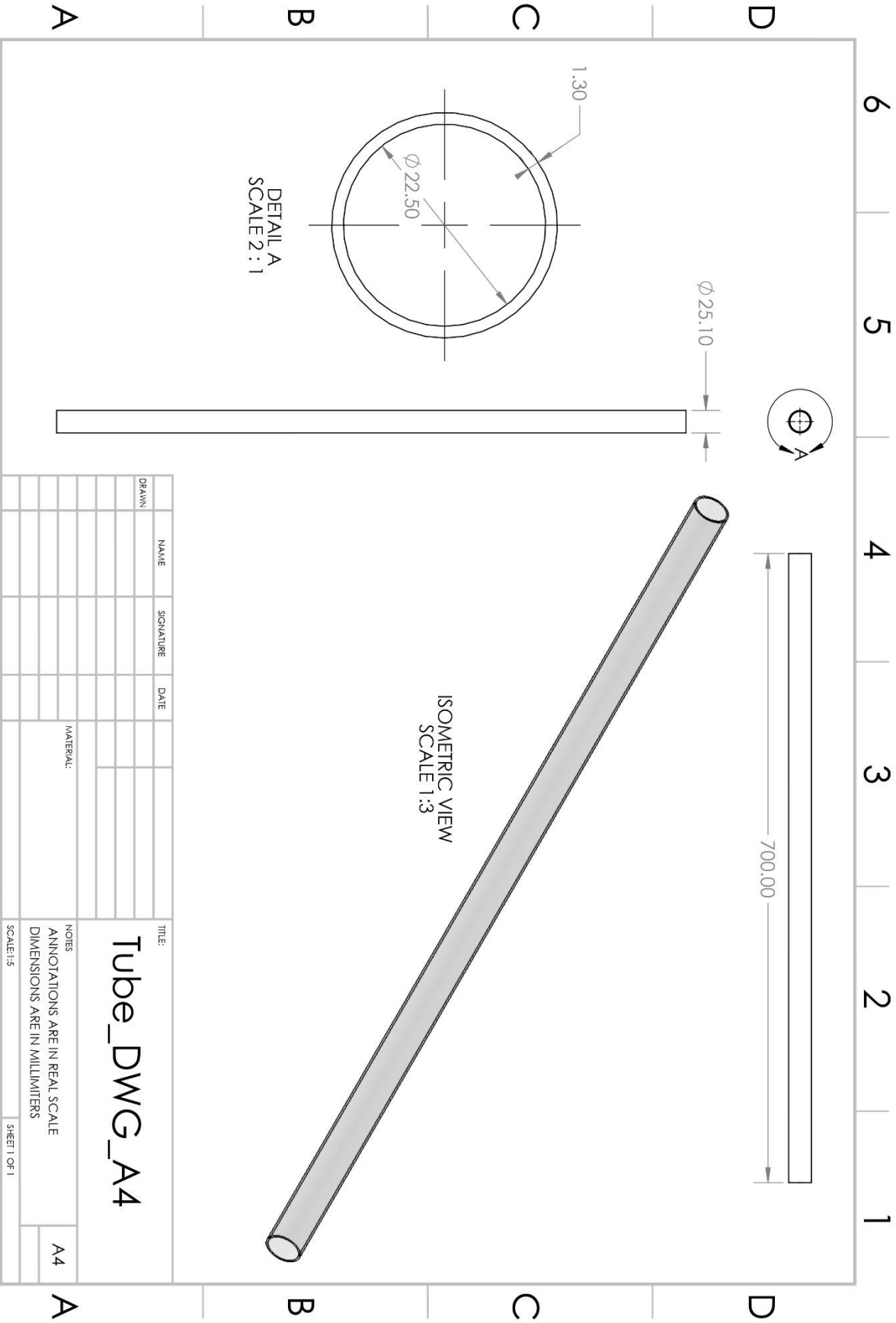
DRAWN	NAME	SIGNATURE	DATE	TITLE:
				G10_DWG_A4
				NOTES ANNOTATIONS ARE IN REAL SCALE DIMENSIONS ARE IN MILLIMETERS SCALE: 1:1
				SHEET 1 OF 1
				A4



SOLIDWORKS Educational Product. For Instructional Use Only.

DRAWN	NAME	SIGNATURE	DATE	TITLE
				<b>Terminations_DWG</b>
				NOTES
				ANNOTATIONS ARE IN REAL SCALE
				DIMENSIONS ARE IN MILLIMETERS
				SCALE: 1:5
				SHEET 1 OF 1

A4



DRAWN	NAME	SIGNATURE	DATE	TITLE:
				<b>Tube_DWG_A4</b>
				NOTES
				ANNOTATIONS ARE IN REAL SCALE
				DIMENSIONS ARE IN MILLIMETERS
				SCALE: 1:5
				SHEET 1 OF 1

# References

- [1] "DEMO," EUROfusion, [Online]. Available: <https://eurofusion.org/programme/demo/>.
- [2] C. Yao and Y. Ma, "Superconducting materials: Challenges and opportunities for large-scale applications," *iScience* 24, 2021.
- [3] R. G. Sharma, Superconductivity Basics and Applications to Magnets, Springer Series in Materials Science 214.
- [4] S. Viarengo, S. Sparacio, L. Savoldi and F. Laviano, *Course of Nuclear Engineering Lab & Advance Heat Transfer Problem - PoliTO*, Torino, 2023.
- [5] H. S. Edelman and D. C. Larbalestier, "Resistive transitions and the origin of the  $n$  value in superconductors with a Gaussian critical-current distribution," *Journal of Applied Physics*, vol. 74, no. 5, pp. 3312-3315, 1993.
- [6] D. M. J. Taylor and D. P. Hampshire, "Relationship between the  $n$ -value and critical current in Nb<sub>3</sub>Sn superconducting wires exhibiting intrinsic and extrinsic behaviour," *Superconductor Science and Technology*, vol. 18, pp. 297-302, 2005.
- [7] R. Musenich, *Course of Applied Cryogenics - INFN*, Genova, 2024.
- [8] Z. S. Hartwig, R. F. Vieira, B. N. Sorbom, R. A. Badcock, M. Bajko, W. K. Beck, B. Castaldo, C. L. Craighill, M. Davies, J. Estrada, V. Fry, T. Golfopoulos, A. E. Hubbard, J. H. Irby, S. Kuznetsov, C. J. Lammi, P. C. Michael, T. Mouratidis, R. A. Murray, A. T. Pfeiffer, S. Z. Pierson, A. Radovinsky, M. D. Rowell, E. E. Salazar, M. Segal, P. W. Stahle, M. Takayasu, T. L. Toland and L. Zhou, "VIPER: An industrially scalable high-current high-temperature superconductor cable," *Superconductor Science and Technology*, vol. 33, no. 11, 2020.
- [9] M. J. Wolf, W. H. Fietz, C. M. Bayer, S. I. Schlachter, R. Heller and K. P. Weiss, "HTS CroCo: A stacked HTS conductor optimized for high currents and long-length production," *IEEE Transactions on Applied Superconductivity*, vol. 26, no. 2, pp. 19-24, 2016.
- [10] L. Muzzi, A. Augieri, G. Celentano, S. Chiarelli, A. della Corte, G. de Marzi, A. di Zenobio, L. Giannini, M. Marchetti, A. Masi, G. Messina, A. Rufoloni, S. Turtu, A. Vannozzi, A. Bragagni, M. Seri, M. Arabi, A. Anemona and A. Formichetti, "Design and Feasibility Assessment of an HTS Sector Shaped High-Current Conductor for

- Fusion Coils," *IEEE Transactions on Applied Superconductivity*, vol. 33, no. 5, 2023.
- [11] V. Corato, *HTS conductor developments for fusion - EUROFUSION*, 2022.
- [12] "Superconductivity," Nexans, [Online]. Available: <https://www.nexans.de/>.
- [13] "ASG Superconductors," ASG Superconductors, [Online]. Available: <https://www.asgsuperconductors.com/>.
- [14] "Superconductors," Luvata, [Online]. Available: <https://www.luvata.com/>.
- [15] M. Eisterer, *HTS versus LTS: physics, technology, and application prospects - EUCAS 2017*, Geneva, 2017.
- [16] "National High Magnetic Field Laboratory," [Online]. Available: <https://nationalmaglab.org/magnet-development/applied-superconductivity-center/plots/>.
- [17] M. Casali, M. Breschi and P. L. Ribani, "Two-dimensional anisotropic model of YBCO coated conductors," *IEEE Transactions on Applied Superconductivity*, vol. 25, no. 1, 2015.
- [18] L. Muzzi, *Superconducting Magnets for Fusion - Seminar within the course on "Nuclear Fusion Reactor Engineering"*, Torino, 2023.
- [19] M. Marchevsky, "Quench detection and protection for high-temperature superconductor accelerator magnets," *Instruments*, vol. 5, no. 3, 2021.
- [20] A. Dudarev, C. Berriaud, F. Broggi, N. Dolgetta, F. P. Juster, M. Tetteroo and H. H. J. ten Kate, "Quench evolution and hot spot temperature in the ATLAS BO model coil," *IEEE Transactions on Applied Superconductivity*, vol. 14, no. 2, pp. 518-521, 2004.
- [21] J. van Nugteren, M. Dhallé, S. Wessel, E. Krooshoop, A. Nijhuis and H. ten Kate, "Measurement and analysis of normal zone propagation in a ReBCO coated conductor at temperatures below 50 K," *Physics Procedia*, vol. 67, p. 945–951, 2015.
- [22] E. E. Salazar, R. A. Badcock, M. Bajko, B. Castaldo, M. Davies, J. Estrada, V. Fry, J. T. Gonzales, P. C. Michael, M. Segal, R. F. Vieira and Z. S. Hartwig, "Fiber optic quench detection for large-scale HTS magnets demonstrated on VIPER cable during high-fidelity testing at the SULTAN facility," *Superconductor Science and Technology*, vol. 34, no. 3, 2021.

- [23] G. Álvarez-Botero, F. E. Barón, C. C. Cano, O. Sosa and M. Varón, "Optical Sensing Using Fiber Bragg Gratings: Fundamentals and Applications," *IEEE Instrumentation & Measurement Magazine*, 2017.
- [24] C. Venditozzi, F. Felli and C. Lupi, "Modeling FBG sensors sensitivity from cryogenic temperatures to room temperature as a function of metal coating thickness," *Optical Fiber Technology*, vol. 42, pp. 84-91, 2018.
- [25] H. Lu, Q. Ni, Y. Hu, Y. Dong, L. Zheng, J. Zhang, Q. Yan, Y. Xiao, T. Wang and H. Liu, "Quench Detection of 20 kA HTS Current Leads Using Distributed Optical Fibers," *IEEE Transactions on Applied Superconductivity*, vol. 34, no. 9, 2024.
- [26] G. Colombo, S. A. Adibi, M. Breschi, M. A. Caponero, A. Castaldo, G. Celentano, A. della Corte, M. Marchetti, A. Masi, C. Mazzotta, L. Muzzi, A. Polimadei, L. Savoldi, A. Trotta, F. Zanon and G. de Marzi, "Fiber-Optics Quench Detection Schemes in HTS Cables for Fusion Magnets," *IEEE Transactions on Applied Superconductivity*, vol. 34, no. 5, pp. 1-5, 2024.
- [27] S. A. Adibi, G. Colombo, M. Breschi, M. A. Caponero, A. Castaldo, G. Celentano, A. della Corte, M. Marchetti, A. Masi, C. Mazzotta, L. Muzzi, A. Polimadei, L. Savoldi, A. Trotta, F. Zanon and G. de Marzi, "Multi-Sensor Quench Detection System for an HTS Slotted Superconducting Cable," *IEEE Transactions on Applied Superconductivity*, vol. 34, no. 3, pp. 1-4, 2024.
- [28] "2G-HTS tapes," Shanghai Superconductor, [Online]. Available: <http://www.shsctec.com/>.
- [29] G. Celentano, G. de Marzi, F. Fabbri, L. Muzzi, G. Tomassetti, A. Anemona, S. Chiarelli, M. Seri, A. Bragagni and A. della Corte, "Design of an industrially feasible twisted-stack HTS cable-in-conduit conductor for fusion application," *IEEE Transactions on Applied Superconductivity*, vol. 24, no. 3, 2014.
- [30] G. de Marzi and et al., "Bending tests of HTS cable-in-conduit conductors for high-field magnet applications," *IEEE Transactions of Applied Superconductivity*, vol. 26, no. 4, 2016.
- [31] H. Bajas, D. Uglietti, C. Muller and K. Sedlak, "Quench Detection and Temperature Measurement With Fiber Optic Sensors," *IEEE Transactions on Applied Superconductivity*, vol. 34, no. 5, pp. 1-5, 2024.
- [32] F. Scurti, J. D. Weiss, D. C. Van Der Laan and J. Schwartz, "SMART conductor on round core (CORC®) wire via integrated optical," *Superconductor Science and Technology*, vol. 34, no. 2, 2021.

- [33] "Theva," Theva, [Online]. Available: <https://www.theva.de>.
- [34] T. Mouratidis and D. G. White, "Performance degradation due to thermal cycling in soldered Faraday and SuperPower HTS tape stacks," *Superconductor Science and Technology*, vol. 37, 2024.
- [35] A. Masi, G. Colombo, M. De Stasio, M. Breschi, M. A. Caponero, G. Celentano, M. Marchetti, L. Muzzi, A. Polimadei, L. Savoldi, A. Trotta, F. Zanon and G. De Marzi, "Integration of Optical Sensors for Quench Detection in HTS Stacks and Cables for Fusion Applications," *IEEE Transactions on Applied Superconductivity*, (submitted).
- [36] National Instruments Corporation, *SCXI-1120/D User Manual*, Austin, TX, USA, 1999.
- [37] "Model 2000 Multimeter User's Manual," Tektronix, [Online]. Available: <https://www.tek.com/en/manual/digital-multimeter/broad-purpose-digital-multimeters-manual-2-keithley-2000-series-6-digit-multimeter-scanning>.
- [38] "Sentea Interrogator," Sentea, [Online]. Available: <https://sentea.com/interrogator>.
- [39] "LakeShore," LakeShore Cryogenics, [Online]. Available: <https://www.lakeshore.com/home>.
- [40] G. Iannone, D. D'Agostino, A. Saggese, G. Celentano and U. Gambardella, "Quench propagation in commercial REBCO composite tapes," *Cryogenics*, vol. 109.
- [41] L. Cavallucci, M. Breschi, P. Luigi Ribani, Q. Zhang and Y. Yang, "Quench in a pancake coil wound with REBCO Roebel cable: Model and validation," *Superconductor Science and Technology*, vol. 34, no. 10, 2021.
- [42] C. Lacroix, J. Giguère, S. M. Bergeron Hartman, G. ben Saad, A. Martin, T. Leduc, M. Gendron-Paul, Z. Bellil, J. H. Fournier-Lupien, L. Moret, P. Barusco, X. Granados, X. Obradors, M. Pekarčíková, F. Gömöry, V. Grosse, M. Bauer and F. Sirois, "Normal zone propagation in various REBCO tape architectures," *Superconductor Science and Technology*, vol. 35, no. 5, 2022.
- [43] C. Lacroix, J. H. Fournier-Lupien, K. McMeekin and F. Sirois, "Normal zone propagation velocity in 2g hts coated conductor with high interfacial resistance," *IEEE Transactions on Applied Superconductivity*, vol. 23, no. 3, 2013.

- [44] G. Iannone, A. Saggese, D. D'Agostino, G. Celentano and U. Gambardella, "Numerical model for quench propagation in composite HTS tapes," *IEEE Transactions on Applied Superconductivity*, vol. 29, no. 5, 2019.